

1 **Assessment of the vulnerability of buildings destroyed during**
2 **postfire debris flow events in Kule village, Yajiang County, China**

3
4 **Author names:**

5 **Jinshui Wang¹², Jiangang Chen^{123*}, Lu Zeng¹², Fei Yang¹², Xiao Li¹², Wanyu**
6 **Zhao¹²³, Huayong Chen¹²**

7
8 **Affiliations**

9 ¹State Key Laboratory of Natural Hazards and Engineering Safety, Institute of Mountain
10 Hazards and Environment, Chinese Academy of Sciences, Chengdu, 610299, China;

11 ²University of Chinese Academy of Sciences, Beijing, 100049, China.

12 ³Sichuan Province Engineering Technology Research Center of Mountain Hazards, Chengdu,
13 610299, China.

14
15 **Corresponding author**

16 Jiangang Chen*

17 Email: chenjg@imde.ac.cn

18

19 **Abstract**

20 Debris flows are frequently triggered by rainstorms after wildfires and pose severe threats
21 to downstream residents and buildings in mountainous regions. However, there has been limited
22 focus on developing a comprehensive framework to assess the physical vulnerability of
23 buildings to postfire debris flows. This study presents a quantitative approach for establishing
24 a physical vulnerability model based on observed building damage and simulated debris flow
25 intensities ~~intensity values~~. Detailed field surveys established a building damage database in
26 Kule village, Yajiang County, ~~to analyse the characteristics of postfire debris flows and establish~~
27 ~~a building damage database~~. Numerical simulations using the FLO-2D model were performed
28 to reproduce the debris flow process and quantify the debris flow intensity, including the flow
29 depth, flow velocity, impact pressure, momentum flux, overturning moment, and relative burial
30 height. Physical vulnerability curves were developed for brick-concrete buildings and
31 compared with those obtained in previous studies, and the differences in vulnerability curves,
32 intensity indicators, and functional models were examined. The results revealed that the
33 lognormal cumulative distribution function (LNCDF) model achieved the best
34 performance, ~~provides the highest statistical significance in terms of the~~ with relative error less
35 than 10% and prediction accuracy exceeding 85%. Critical thresholds for complete building
36 damage were identified as a flow depth of 2.5 m and impact pressure of 25 kPa. The momentum
37 flux demonstrated greater sensitivity in distinguishing different damage categories, whereas the
38 impact pressure provided more precise vulnerability index predictions. The proposed physical
39 vulnerability model can ~~be used to~~ evaluate the building structural resistance ~~of buildings~~ to

40 debris flows in wildfire-affected areas, ~~thus~~ providing a systematic foundation for **formulating**
41 risk management and mitigation strategies.

42 **Keywords:** Postfire debris flow, Vulnerability, Building damage, Emergency evacuation

43 **1. Introduction**

44 Debris flows are recurring and destructive hazards in mountainous regions, posing
45 significant threat to downstream buildings and human lives (Cui et al., 2018; Chen et al., 2021).

46 Recently, debris flow disasters after wildfires have received widespread attention, as wildfires
47 increase debris flow susceptibility by reducing vegetation cover, altering soil hydrology, and
48 lowering rainfall thresholds for initiation (Kean et al., 2019; Thomas et al., 2023; Ouyang et al.,
49 2023). These effects can persist for years and generate larger events compared to unburned
50 conditions, amplifying risks to downstream communities (Gorr et al., 2023; Vahedifard et al.,
51 2024). Destructive postfire debris flow events such as the 2018 Montecito, California disaster
52 (23 fatalities, >400 buildings damaged), the 2021 Muli County, China event (186 houses
53 destroyed), and the 2024 Yajiang County, China event highlight the urgent need for
54 vulnerability assessment (Kean et al., 2019; Ouyang et al., 2023; He et al., 2024). However, a
55 comprehensive framework for assessing physical vulnerability of buildings to postfire debris
56 flows remain limited.

57 Assessing building vulnerability to debris flows is essential for risk assessment, emergency
58 evacuation, disaster reduction and rural planning (Eidsvig et al., 2014; Zhang et al., 2018; Wang
59 et al., 2024). Physical vulnerability is defined as the expected degree of loss to structures under
60 a given hazard intensity (Fuchs et al., 2007; Papathoma-Köhle et al., 2021). Over the past two

61 decades, building vulnerability assessments have transitioned from qualitative approaches to
62 quantitative methods, specifically data-driven and mechanism-based models (Luo et al., 2023).
63 These methods are commonly represented through three primary tools for debris flow
64 vulnerability: matrices, indicators, and curves (Papathoma-Köhle et al., 2017).~~Overall, in~~
65 ~~natural hazard research, vulnerability often refers to physical vulnerability (Fuchs et al., 2007),~~
66 ~~which refers to the degree of expected loss of physical structures resulting from a hazard event~~
67 ~~of a given intensity (Chen et al., 2021; Papathoma-Köhle et al., 2022). Over the past two~~
68 ~~decades, building vulnerability assessments have transitioned from qualitative approaches, such~~
69 ~~as experience and indicator based models, to quantitative methods, including data-driven and~~
70 ~~mechanism-based models (Luo et al., 2023). Papathoma-Köhle et al. (2017) identified three~~
71 ~~primary methods for representing physical vulnerability to debris flows: vulnerability matrices,~~
72 ~~indicators, and curves.~~ Among these methods, vulnerability curves are widely employed to
73 quantify the relationship between the debris flow intensity and the extent of building damage
74 (Zhang et al., 2018; Luo et al., 2020). With increasing hazard intensity, the degree of damage
75 follows a monotonically increasing curve~~continuous curve~~ (Lee et al., 2024), ranging in value
76 from 0 (no damage) to 1 (complete damage), as determined via the data-driven approach.
77 Several statistical method-based studies have been conducted to develop physical vulnerability
78 curves for debris flows on the basis of field data (Lee et al., 2024). They have established curves
79 based on intensity-damage relationships (Fuchs et al., 2007; Totschnig et al., 2011) for specific
80 regions and building types like brick-concrete (BC) and reinforced concrete (RC) structures
81 (Kang and Kim, 2016)~~Fuchs et al. (2007) established a vulnerability curve for brick-concrete~~

82 ~~(BC) buildings to describe the relationship between the degree of damage and the debris flow~~
83 ~~intensity, which has been documented extensively. Moreover, Totschnig et al. (2011) studied~~
84 ~~three debris flow events and established vulnerability curves on the basis of the damage ratio~~
85 ~~of the flow depth to the building height. Kang and Kim (2016) developed vulnerability~~
86 ~~functions for different building structure types in Korea, including reinforced concrete (RC)~~
87 ~~and non-RC structures.~~

88 However, in many regions, the availability of debris flow data is often limited because of
89 the infrequent occurrence of significant debris flow events (Navratil et al., 2013; Wang et al.,
90 2024). Moreover, although valuable debris flow intensity-related data are regularly collected
91 (Marchi et al., 2002), few studies have focused on monitoring the impact of debris flows on
92 buildings (Jakob et al., 2012). Therefore, dynamic numerical models have increasingly been
93 employed to reconstruct debris flow processes and determine the hazard intensity (Zhang et al.,
94 2018; Ouyang et al., 2019; Chang et al. 2020). Such runout models play a critical role in
95 bridging data gaps (Chen et al., 2021) and can serve as inputs for vulnerability functions to
96 predict building damage (Barnhart et al., 2024). In prior studies, different numerical simulation
97 models have been used to develop vulnerability curves and evaluate building damage (Luo et
98 al., 2023), including Flow-R, RAMMS, FLO-2D, and D-Claw (Lee et al., 2024; Barnhart et al.,
99 2024). Among these numerical models, FLO-2D has been the most frequently utilized (Quan
100 Luna et al., 2011; Zhang et al., 2018; Chen et al., 2021; Wang et al., 2024). Previous studies
101 using FLO-2D have developed vulnerability curves for multiple intensity indicators, including
102 flow depth, velocity, impact pressure, momentum flux, overturning moment, and relative burial

103 [height, across different building types such as brick-concrete, reinforced concrete, and masonry](#)
104 [structures](#). Lee et al. (2024) proposed a vulnerability curve of the impact pressure for brick
105 masonry buildings in South Korea via the use of Flow-R simulation software. Barnhart et al.
106 (2024) compared the effectiveness levels of two hazard intensity indicators (the flow depth and
107 the momentum flux) alongside three runout models (the Rapid Mass Movement Simulation
108 (RAMMS), FLO-2D, and D-Claw models) and applied them to obtain probabilistic forecasts
109 of wood-framed building damage. Each numerical model exhibits unique advantages and
110 tailored applications, with the FLO-2D model as the most frequently utilized option (Quan Luna
111 et al., 2011; Zhang et al., 2018; Chen et al., 2021; Wang et al., 2024). Specifically, Quan Luna
112 et al. (2011) developed vulnerability curves for the flow depth and impact pressure using the
113 FLO-2D model. Zhang et al. (2018) established six vulnerability curves via FLO-2D numerical
114 modelling, including the flow depth, flow velocity, impact pressure, momentum flux,
115 overturning moment, and relative intensity, to assess debris flow-induced damage to BC and
116 RC buildings in Zhouqu County, China. Chen et al. (2021) proposed a momentum flux curve
117 for masonry wood and BC buildings in Cutou Gully, Wenchuan County, China, on the basis of
118 FLO-2D simulations of debris flows. Wang et al. (2024) developed vulnerability curves for the
119 flow depth and impact pressure using FLO-2D model simulations suitable for the
120 Wangzhuangwu watershed, Zhejiang Province, China. Notably, the accuracy of this numerical
121 model highly depends on the selection of parameter values (Chen et al., 2021), which requires
122 a comprehensive understanding of debris flow properties, including their formation
123 mechanisms, frequency, and intensity (Chang et al., 2020). Furthermore, accurately calculating

124 the debris flow volume (Barnhart et al., 2024) and the peak discharge (Wang et al., 2024) is
125 critical for ensuring the reliability of runoff dynamics prediction outcomes.

126 In addition, the uncertainty and accuracy of vulnerability curves are affected not only by
127 the adopted numerical model but also by the debris flow intensity and building damage
128 attributes, as well as the statistical functional models linking the two (Luo et al., 2023; Lee et
129 al., 2024). First, there are numerous intensity indicators, including the two easily obtained direct
130 parameters quantities of the flow depth and velocity (Eidsvig et al., 2014; Kang and Kim, 2016;),
131 as well as derivative parameters, such as the impact pressure (Quan Luna et al., 2011; Lee et
132 al., 2024; Wang et al., 2024), momentum flux (Jakob et al., 2012; Ouyang et al., 2019; Chen et
133 al., 2021; Barnhart et al., 2024), overturning moment (Zhang et al., 2018), and relative burial
134 height (Totschnig et al., 2011; Zhang et al., 2018). Second, various factors related to buildings
135 can significantly influence vulnerability assessments, including building features such as the
136 number of floors, direction, shielding effects and construction codes (Luo et al., 2020), as well
137 as the building structure type such as wood-frame buildings, masonry buildings, BC buildings,
138 and RC buildings, which have been studied extensively (Lee et al., 2024). Additionally, building
139 damage due to debris flows has been primarily classified qualitatively (Hu et al., 2012). Within
140 this framework, the damage state is commonly categorized as slight, moderate, extensive, and
141 complete damage (Luo et al., 2023). Third, vulnerability curves can be fitted using several
142 functional models (Luo et al., 2023), such as polynomial functions, logistic functions, Weibull
143 distributions, exponential functions, lognormal cumulative distribution function (LNCDF) and
144 Avrami functions (Fuchs et al. 2007; Quan Luna et al., 2011; Eidsvig et al., 2014; Luo et al.,

145 2023; Lee et al., 2024). Thus, further research remains needed to determine the most reliable
146 predictions on the basis of different vulnerability functions and hazard intensity measures.

147 In this study, the aim was to comprehensively assess the physical vulnerability of buildings
148 damaged during postfire debris flows in Kule village, Yajiang County. The primary objectives
149 are as follows: (1) To analyze the characteristics of postfire debris flows and establish a building
150 damage database through field investigations. (2) To reconstruct debris flow events via FLO-2D
151 numerical simulations in order to determine debris flow intensity. (3) To develop physical
152 vulnerability curves for BC buildings for assessing the establishment and application of a
153 vulnerability assessment model. (4) To compare the differences in performance among various
154 vulnerability approaches, such as existing intensity indicators, curves, and function models.
155 This work aims to provide insights for advancing postfire debris flow assessments, improving
156 vulnerability models, and guiding emergency evacuation efforts in this region.~~The primary~~
157 ~~objectives were as follows: (1) The characteristics of postfire debris flows were analysed, and~~
158 ~~a building damage database was established through field investigations. (2) Debris flow events~~
159 ~~were reconstructed via FLO-2D numerical simulations to determine the debris flow intensity.~~
160 ~~(3) Physical vulnerability curves were developed for BC buildings to assess the establishment~~
161 ~~and application of a vulnerability assessment model. (4) The differences in performance among~~
162 ~~various vulnerability approaches, such as existing intensity indicators, curves and function~~
163 ~~models, were compare _~~

164 2. Methods

165 The methodological procedure in this study is divided into four steps (Fig. 1). In step 1,

166 we conducted a field investigation and obtained images of burned areas, channel morphology,
167 grain size distribution, and features of buildings in gullies affected by debris flows (Fig. 4).
168 Then, we calculated the physical characteristic parameters of postfire debris flows. Finally, we
169 reproduced and predicted dynamic runout processes via numerical simulations using the FLO-
170 2D model. In step 2, we employed a numerical model to calculate six indicators of the debris
171 flow intensity (Zhang et al., 2018). Moreover, the damage degree of buildings was classified,
172 and vulnerability index values were assigned on the basis of the degree of damage to buildings
173 (Wang et al., 2024). In step 3, we established building vulnerability curves and a function model
174 using the reconstructed debris flow intensity and building damage information from the G1
175 gully (after postfire debris flow occurrence). We subsequently applied the vulnerability model
176 to predict potential future scenarios of building damage in the G2 gully (under potential future
177 debris flow scenarios), aiming to assess the compound, bilateral threat that both gullies pose to
178 the downstream Kule Village community. Finally, in step 4, we verified and compared the
179 performance of the proposed vulnerability model with that of previous models and provide
180 suggestions for emergency response and evacuation routes during disasters in Kule village. This
181 methodology facilitates a comprehensive analysis of the potential effects of future postfire
182 debris flow events on buildings within the region, offering valuable insights for formulating
183 disaster management and mitigation strategies.

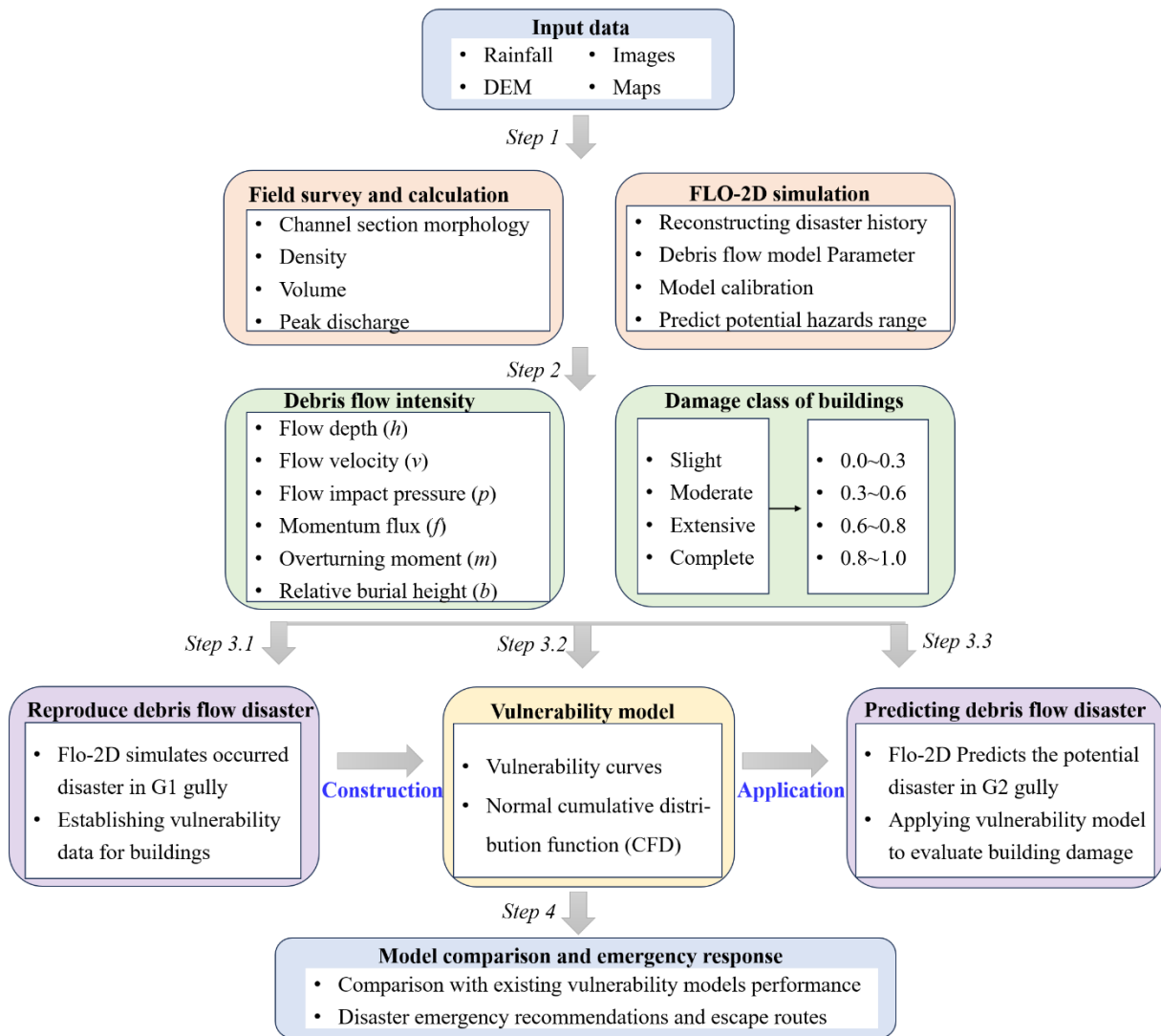


Figure 1. Methodological framework

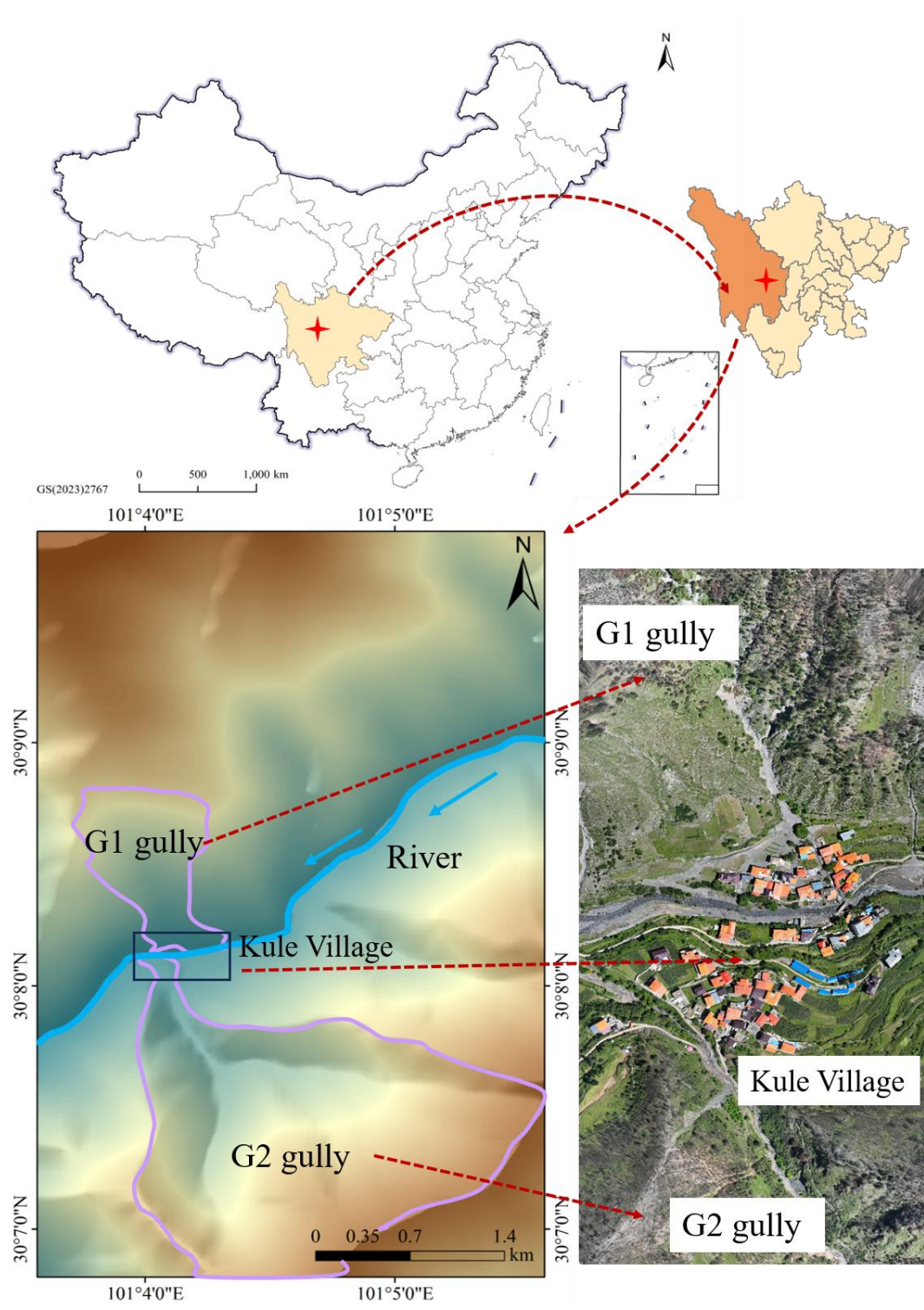
2.1. Field investigation and data acquisition

2.1.1 Study area

The study area is located in Yajiang County, Sichuan Province, China. Yajiang County occurs in the southeastern part of the Qinghai–Tibet Plateau and the central segment of the Hengduan Mountains within the basin of the Yalong River (He et al., 2024). The Kule watershed (coordinates: 101°4'12.53" E, 30°7'55.88" N) is located in the northeastern part of Xiala town in Yajiang County, and the terrain encompasses mainly high mountains and deep canyons. The

193 study area of the Kule watershed contains two primary gullies (G1 and G2), which converge
194 with the main river in the downstream impact area of Kule village (Fig. 2). Kule village contains
195 58 households with 308 people, and the Kule River flows through the downstream alluvial fan
196 of this village. The left and right banks of the village are impacted by the G1 and G2 gullies,
197 respectively. The catchments of the G1 gully and G2 gully cover areas of 1.4 and 3.5 km²,
198 respectively, and the terrain elevation differences range from 850~1,015 m. Geologically, the
199 area primarily comprises Late Triassic silty slate. The bedrock is severely weathered and
200 structurally fragmented. Within the catchment, the bedrock is overlain by Quaternary sediments
201 that are approximately 1.0~3.0 m thick (He et al., 2024). The thin residual soil layer is
202 susceptible to failure during periods of intense rainfall.

203 On 15 March, 2024, a wildfire ignited in Yajiang County, burning 278.8 km² of
204 mountainous forest and affecting 250 watersheds, with moderate-high burn levels accounting
205 for more than 50% of the total catchment area (He et al., 2024). Several postfire debris flows
206 occurred in the burned catchments on May 10 that were induced by rainfall events following
207 the fire. In particular, the postfire debris flows in the G1 gully in Kule village destroyed 36
208 houses, blocked roads, and displaced people. Postfire debris flow and building damage data
209 were collected from this event to support building vulnerability assessment and disaster
210 reduction efforts (Zhang et al., 2018; Gorr et al., 2023).

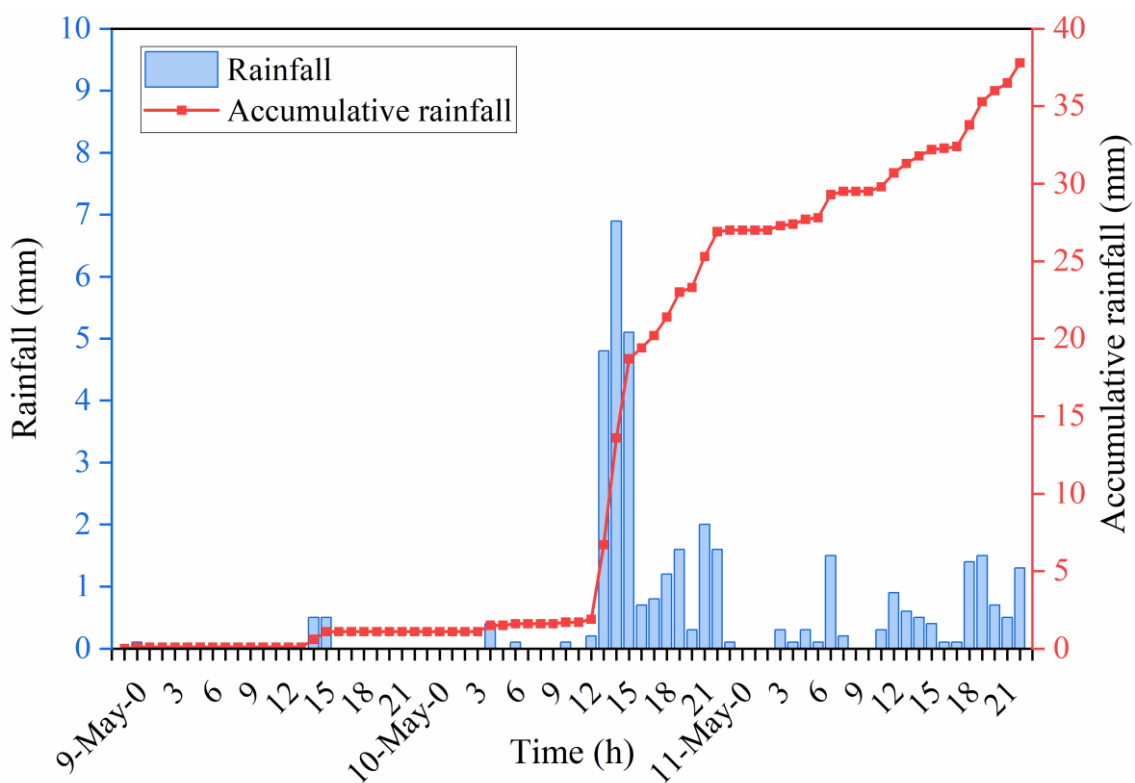


211

212 [Figure 2. Location of the study area in the Kule Gully, Yajiang County, Sichuan Province, China.](#)

213 [Yajiang County occurs in a plateau monsoon climate zone, and the long-term annual](#)
 214 [precipitation ranges from 600 to 1200 mm, with precipitation mainly concentrated from June](#)
 215 [to September, , which accounts for about 86% of the annual total, with a recent decadal average](#)

216 (2010–2020) of 705 mm. The rainstorm started at 14:00 on 10 May and lasted until 11 May,
 217 according to records from a rainfall monitoring station (coordinates: 101°1'20" E, 30°1'57" N).
 218 The maximum recorded hourly rainfall intensity was 6.9 mm/h, and the accumulated rainfall
 219 reached 37.8 mm (Fig. 3). Notably, the rainfall threshold of postfire debris flows is much lower
 220 than that of nonfire debris flows (Ouyang et al., 2023). In particular, low-intensity rainfall can
 221 trigger postfire debris flows in the G1 gully, and the G2 gully occurs in a state in which debris
 222 flows can occur at any time. Owing to wildfires, a large amount of loose material remains on
 223 hillslopes and in channels, which can provide abundant material sources for triggering debris
 224 flows (McGuire et al., 2024). Thus, debris flow activity in the G1 and G2 gullies may last longer.

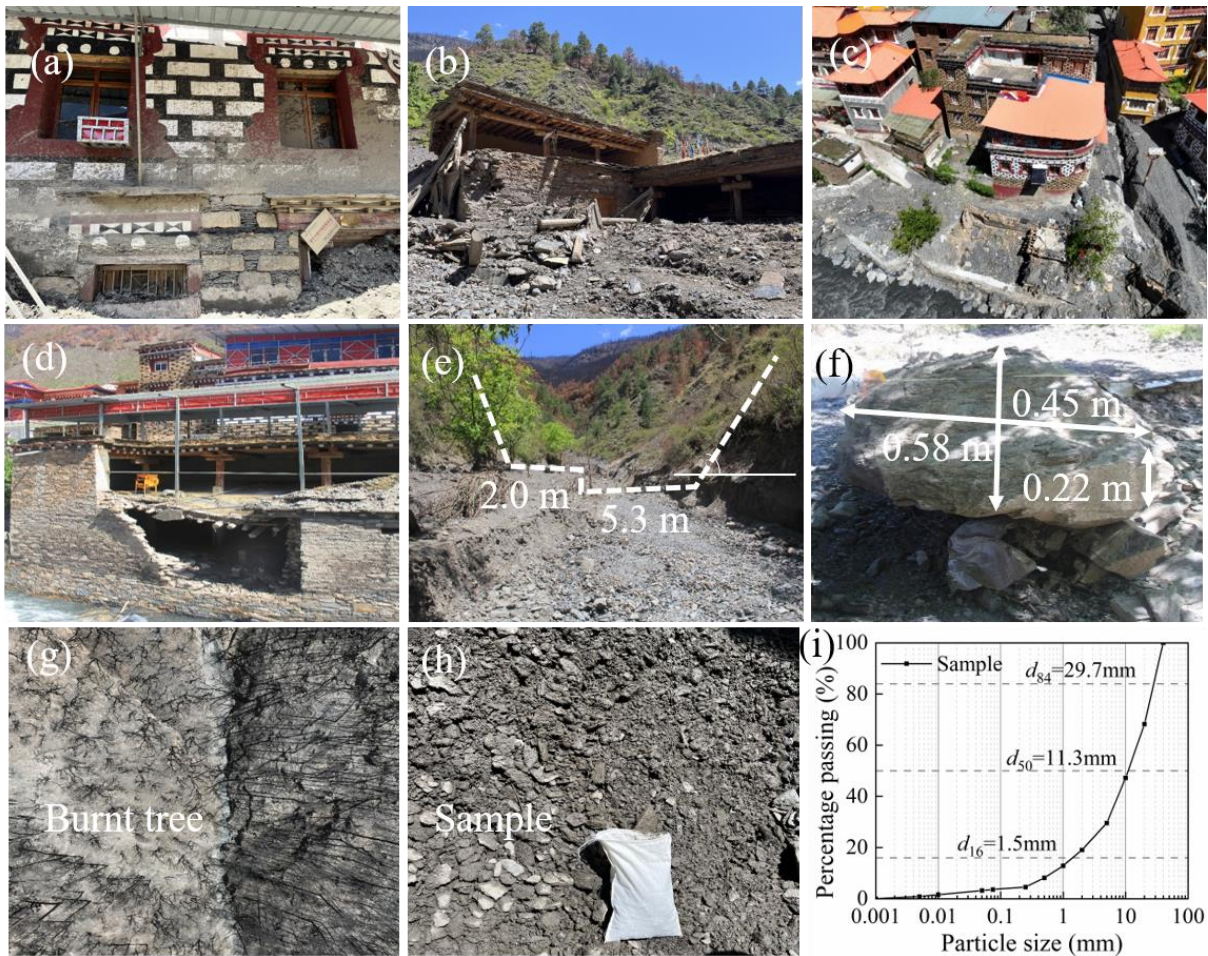


225
 226 Figure 3. Hydrological characteristics: distributions of the hourly and cumulative rainfall levels.

227 **2.1.2 Field data collection**

228 An unmanned aerial vehicle (UAV) (Inspire3, DJI-Innovations; vertical accuracy: ± 0.1 m;

229 horizontal accuracy: ± 0.3 m) was employed to obtain images of the G1 and G2 gullies, which
230 were used to acquire topographic and geomorphic information of channels and the spatial
231 distribution of buildings (Fig. 5). A laser rangefinder (Contour XLRic, with a maximum range
232 of 1,850 m and a measurement accuracy of 0.10 m) was applied to measure the dimensions of
233 buildings (floor height, width, and length) and the section size of channels (width, gully bed
234 gradient, and bank slope angle) (Fig. 4). The structural type, impact azimuth, affected portion
235 and damage degree of the building were recorded with a camera (SONY A6400). The size of
236 stone blocks, thickness of the ash layer and burned soil, burial height and flow depth mark were
237 measured with a scale. The particle size of postfire debris flows was measured with vibrating
238 sieving machines (measuring range: 0.25~20 mm) and Malvern particle size analysers
239 (measuring range: 0.02-2,000 μm ; scanning speed: 1,000 Hz). Then, the samples were analysed
240 to obtain particle size distribution curve~~a percentage passing curve~~. Derived from sieving and
241 laser analysis, the curve only includes particles up to 20 mm and excludes the larger boulders
242 documented in the field (Fig. 4f). Field work served as the basis for the subsequent simulations
243 and the determination of postfire debris flow physical parameters.



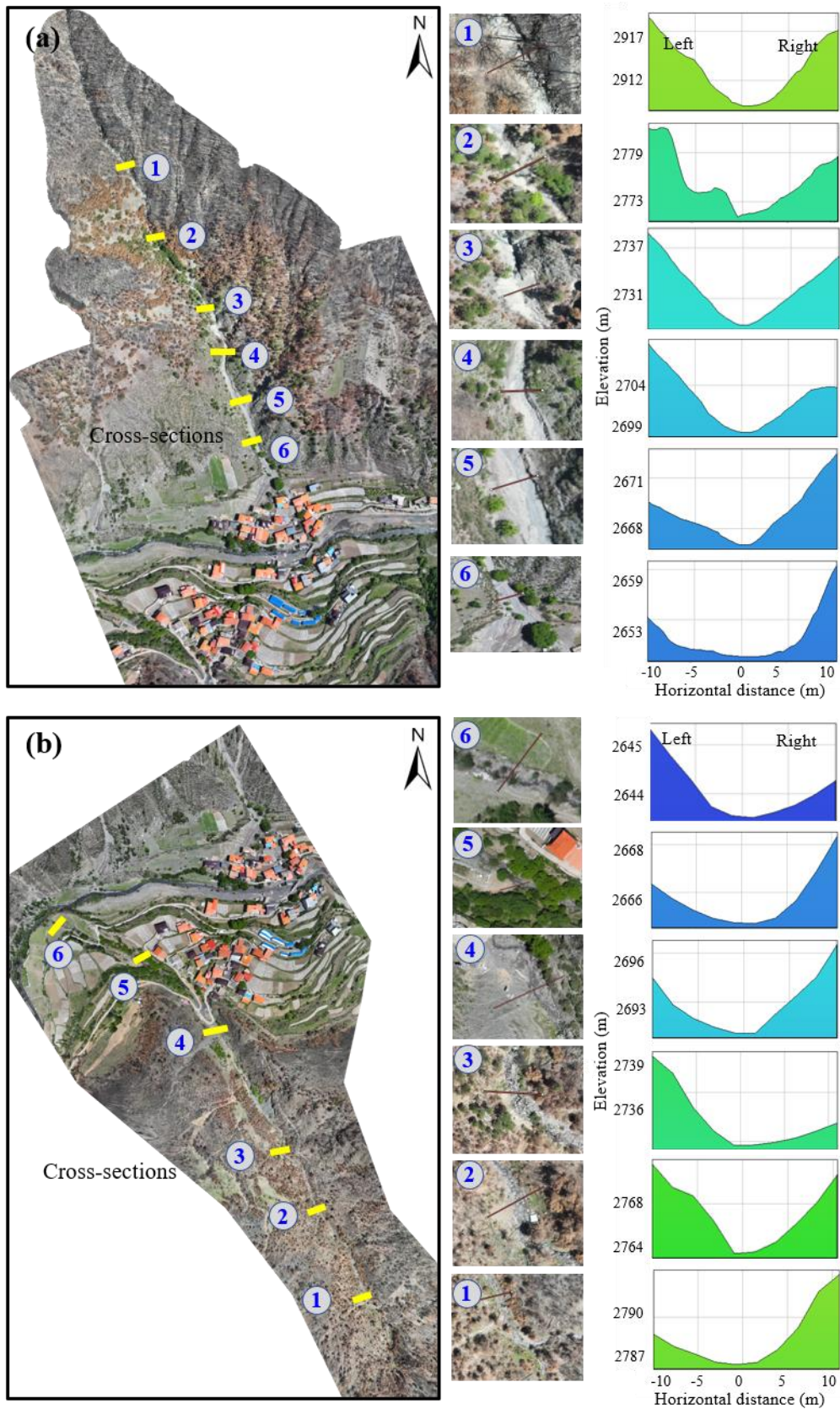
244
 245 Figure 4. Fieldwork techniques for capturing postfire debris flow events: (a)-(d) Damaged
 246 buildings; (e) channel section; (f) block stone size; (g) burned area; (h) particle sampling; (i)
 247 particle size distribution curve.

248 The obtained aerial images were subsequently processed using PhotoScan software to
 249 generate a 3D digital orthophoto in the WGS-1984 geographic coordinate system (Wang et al.
 250 2024) and to produce a digital elevation model (DEM), which served as base data for the
 251 subsequent runout analyses. These digital model data facilitated the identification of
 252 geomorphic features within the G1 and G2 catchments and the spatial distribution of damaged
 253 buildings (Fig. 5). The G1 and G2 gullies are located on the left and right banks of Kule village,
 254 respectively. [G1 and G2 are spatially adjacent and exhibit similarities in terms of geological](#)

255 [setting, soil type, vegetation, catchment hydrological characteristics, fire history, and field-](#)
 256 [observed surface material composition.](#) The catchment area of the G1 gully is small, but the
 257 longitudinal gradient of the main channel is [steeper](#)~~high~~, with extensive moderate-high burned
 258 areas (He et al., 2024). The catchment area of the G2 gully is large, with a [gentler](#)~~lower~~
 259 longitudinal gradient of the main channel and a larger relative terrain elevation difference. Six
 260 cross-sectional channel measurements (from sections 1 to 6) revealed that the channel width
 261 gradually increases from upstream to downstream, ranging from 2 to 10 m (Fig. 5). The
 262 characteristic parameters of the G1 and G2 gullies are listed in Table 1.

263 Table 1 Characteristics of the G1 and G2 gullies on both sides of Kule village, Yajiang County

Debris flow gully	Catchment area (km ²)	Main channel length (km)	Average slope of the channel	Burned area (km ²)	Watershed relief (m)	Relative position	Debris flow event
G1 gully	1.40	1.60	0.40	0.90	850.00	Left bank of Kule village	Debris flows occurred
G2 Gully	3.50	2.20	0.17	1.50	1,015.00	Right bank of Kule village	Debris flows may occur



264

265 Figure 5. Characteristics of different channel cross sections: (a) G1 debris flow channel on the

266 left bank of Kule village; (b) G2 debris flow channel on the right bank of Kule village.

267 2.1.3 Calculation of postfire debris flow parameters

268 (1) Debris flow density

269 The particle size distribution of a given debris flow deposit can be used to determine the
270 debris flow density, which can be calculated as follows (Wang et al., 2024; Chen et al., 2021):

$$271 \quad \gamma_d = \gamma_0 + \gamma_m P_2 (P_{0.05})^{0.35} \quad (1)$$

272 where γ_d is the density of the debris flow (t/m^3); γ_m is the minimum density of a
273 viscous debris flow (2.0 t/m^3); γ_0 is the minimum density of the debris flow ($1.4\sim 1.5 \text{ t/m}^3$); P_2
274 is the percentage of coarse particles with a diameter greater than 2 mm; and $P_{0.05}$ is the
275 percentage of fine particles with a diameter smaller than 0.05 mm.

276 (2) Debris flow volume

277 The US Geological Survey (USGS) debris flow hazard assessment system is based on a
278 model developed by Gartner et al. (2014) for estimating the volume of postfire debris flows.
279 The emergency assessment volume model is a multiple linear regression model and has been
280 widely applied (Rengers et al., 2023; Gorr et al., 2024). This model can be expressed as follows:

$$281 \quad \ln(V_{DF}) = 4.22 + 0.39\sqrt{I_{15}} + 0.36\ln(B_{mh}) + 0.13\sqrt{R} \quad (2)$$

282 where V_{DF} is the postfire debris flow volume (m^3); I_{15} is the 15-min maximum rainfall
283 intensity (mmh^{-1}); B_{mh} is the burned area with moderate and high burn severity levels (km^2);
284 and R is the watershed relief (m).

285 (3) Debris flow peak discharge

286 The debris flow peak discharge can be estimated via the volume-peak discharge
287 relationship method (Rickenmann 1999; Marchi et al., 2002) or the rain-flood method (Zhou et

288 al., 1991; Cui et al., 2023).

289 First, the peak discharge for a given catchment can be estimated on the basis of the debris
290 flow volume (Kang and Kim, 2016). Notably, studies have demonstrated that the debris flow
291 volume is related to the peak discharge (Navratil et al., 2013; Cui et al., 2018; Guo et al., 2024):

$$292 \quad Q_d = \alpha V_{DF}^\beta \quad (3)$$

293 where Q_d is the peak discharge of the debris flow (m^3/s); V_{DF} is the postfire debris flow
294 volume (m^3), which can be calculated by Eq. (2); and α and β are fitting coefficients for different
295 watersheds, with a specific range. Please refer to Guo et al. (2024) for further details.

296 Second, the rain-flood method can be used for calculating rainfall-triggered debris flows
297 under different rainfall frequency conditions (Zhou et al., 1991; Chang et al., 2020):

$$298 \quad Q_d = (1 + \phi) Q_f D_u \quad (4a)$$

299 where Q_f is the peak flood discharge of clean water (m^3/s); Q_d is the peak flow of the debris
300 flow (m^3/s); D_u is the blockage amplification factor; ϕ is the solids concentration, $\phi = (\gamma_d - 1) / (\gamma_s -$
301 $\gamma_d)$; and γ_d and γ_s are the densities of the debris flow and solid materials (t/m^3), respectively.

$$302 \quad Q_f = 0.278 \phi \frac{S}{\tau^n} F \quad (4b)$$

303 where ϕ is the peak runoff coefficient; S is the storm force (mm/h), namely, the maximum
304 1-h rainstorm intensity; τ is the confluence time (h); n is the rainstorm attenuation index; and F
305 is the watershed area (km^2). The parameters in Eq. (4b) can be obtained by consulting the
306 calculation manual and can be calculated as follows (Sichuan Hydrological Manual 1984; Cui
307 et al., 2023):

$$308 \quad \phi = 1 - 1.1 \frac{\mu}{S} t_0^n \quad (5a)$$

309 $S = H_1 K_1$ (5b)

310 $t = t_0 \rho^{-\frac{1}{4-n}}$ (5c)

311 $n = 1 + 1.285 \left(\lg \frac{H_1 K_1}{H_6 K_6} \right)$ (5d)

312 $\mu = 3.6 K_p F^{-0.19}$ (5e)

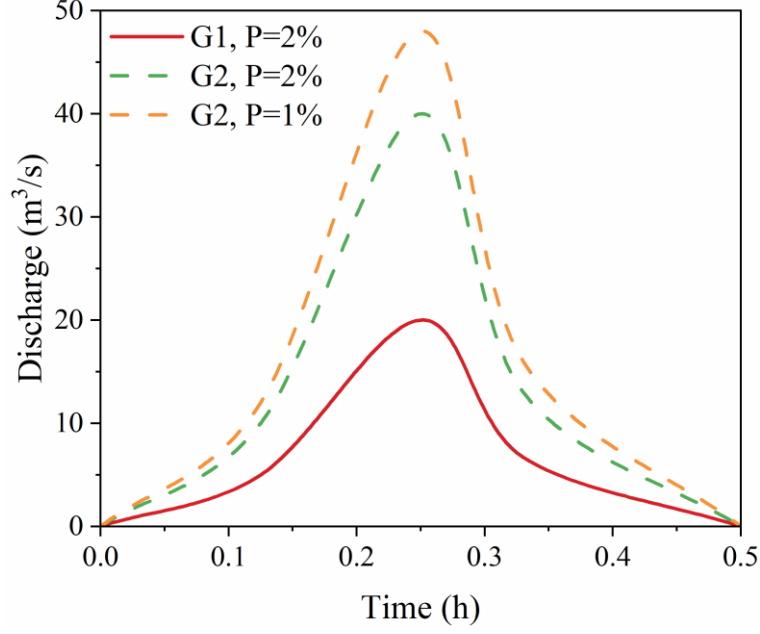
313 $t_0 = \left(\frac{0.383}{m S^{1/4} / \theta} \right)^{\frac{4}{4-n}}$ (5f)

314 $m = 0.221 \theta^{0.204}$ (5g)

315 $\theta = \frac{L}{J^{1/3} F^{1/4}}$ (5h)

316 where μ is the current generation parameter (mm/h); t_0 is the confluence time of the basin;
 317 H_1 and H_6 are the 1- and 6-h average rainfall amounts, respectively (mm); K_1 and K_6 are the
 318 modulus coefficients corresponding to periods H_1 and H_6 , respectively; K_p is the modulus ratio
 319 coefficient of the Pearson curve; m is the confluence parameter; θ is the watershed coefficient;
 320 J is the slope of the channel; and L is the main channel length (km).

321 Finally, we combined the results of the two peak discharge calculation methods to
 322 determine the peak discharges of the postfire debris flows in the G1 and G2 gullies at different
 323 frequencies (Fig. 6). [The flow process line of debris flow discharge can be obtained by using](#)
 324 [the generalized pentagon method, which has been widely adopted in previous studies \(Zhang](#)
 325 [et al., 2023; Ding et al., 2023\).](#)



326

327 Figure 6. Flow hydrographs of the G1 and G2 gullies at different frequencies.

328 2.2 FLO-2D numerical simulation of disaster scenarios

329 2.2.1 Governing equations for rainfall runoff and debris flows

330 The two-dimensional numerical debris flow evolution model FLO-2D was applied to
 331 simulate the runout process and to quantify key metrics of debris flows in the G1 and G2 gullies
 332 (Wang et al., 2024; Si et al., 2022; Zhang et al., 2018; Chang et al., 2020). On the basis of 2D
 333 shallow water equations, mass and momentum conservation equations are employed in the
 334 FLO-2D model as the governing equations:

$$335 \quad i = \frac{\partial h}{\partial t} + \frac{\partial h \partial V_x}{\partial x} + \frac{\partial h \partial V_y}{\partial y} \quad (6a)$$

$$336 \quad S_{fx} = S_{ox} - \frac{\partial h}{\partial x} - \frac{V_x}{g} \frac{\partial V_x}{\partial x} - \frac{V_y}{g} \frac{\partial V_x}{\partial y} - \frac{1}{g} \frac{\partial V_x}{\partial t} \quad (6b)$$

$$337 \quad S_{fy} = S_{oy} - \frac{\partial h}{\partial y} - \frac{V_y}{g} \frac{\partial V_y}{\partial y} - \frac{V_x}{g} \frac{\partial V_y}{\partial x} - \frac{1}{g} \frac{\partial V_y}{\partial t} \quad (6c)$$

338 where h is the flow depth; V_x and V_y are the depth-averaged velocities along the horizontal

339 x and y coordinates, respectively; i is the intensity at the flow surface; and S_{fx} and S_{fy} are the
 340 friction slopes, expressed as functions of bed slopes S_{ox} and S_{oy} , respectively, the pressure
 341 gradient and the convective and local acceleration terms (Chen et al., 2021). The total friction
 342 slope, S_f , is the sum of the yield slope, the viscous slope, and the turbulent dispersive slope
 343 (Zhang et al., 2018), which can be obtained as follows:

$$344 \quad S_f = \frac{\tau_y}{\gamma_m h} + \frac{K\eta v}{8\gamma_m h^2} + \frac{n^2 v^2}{h^{4/3}} \quad (7)$$

345 where n is Manning's coefficient; K is flow resistance parameter; η is the dynamic viscosity
 346 (Pa·s), and τ_y is the yield stress (Pa), which can be calculated as follows:

$$347 \quad \eta = \alpha_1 e^{\beta_1 C_v} \quad (8a)$$

$$348 \quad \tau_y = \alpha_2 e^{\beta_2 C_v} \quad (8b)$$

349 where C_v is the sediment concentration, and α_1 , α_2 , β_1 , and β_2 are empirical coefficients.

350 The FLO-2D simulations were conducted by adding elevation data of the computation area
 351 to the grid, which was set to 5 m×5 m, after which the inlet and outlet conditions, the rheological
 352 parameters (Table 2), the duration of the debris inflow hydrograph (i.e., 30 min) and the peak
 353 discharge were defined. Finally, the dynamics and key parameters, such as the flow depth and
 354 flow velocity, were obtained.

355 Table 2. the rheological parameters for the debris flow simulation.

Parameters	Value
Manning's roughness coefficient (n)	0.10
Flow resistance parameter (K)	2,280
Sediment concentration (C_v)	0.49
Viscosity coefficients α_1	0.81

	β_1	13.72
Yield stress coefficients	α_2	0.00462
	β_2	11.24

356 2.2.2 Model calibration and validation

357 To ensure accuracy, the methodology proposed by Scheidl and Rickenmann (2010) was
358 adopted to validate the simulation results (Table 3). We measured the observed depositional fan
359 area through field investigations and the predicted depositional fan area obtained with the FLO-
360 2D model (Chen et al., 2021). The subareas (X, Y and Z) were obtained via the overlay of the
361 predicted deposition area with the observed deposition area. We assessed the overall
362 reconstruction accuracy via the following evaluation parameters (Chen et al., 2021; Wang et al.,
363 2024):

$$364 \quad \varepsilon = \frac{S_X}{S_{observed}} - \frac{S_Y}{S_{observed}} - \frac{S_Z}{S_{observed}} + \frac{V_X}{V_{observed}} \quad (9)$$

$$365 \quad \delta = \frac{\varepsilon + 2}{4} \quad (10)$$

366 where S_X , S_Y , and S_Z are the positive accuracy region, negative accuracy region, and
367 missing accuracy region, respectively; $S_{observed}$ is the actual impact zone; V_X is the correct
368 judgement volume; $V_{observed}$ is the actual volume; and δ is the normalized accuracy value, with
369 values ranging from 0 to 1.

370 Table 3 Calibration parameters and accuracy of the numerical simulation results

Parameters	S_X	S_Y	S_Z	$S_{observed}$	V_X	$V_{observed}$	ε	δ
	(10^3 m^2)	(10^3 m^2)	(10^3 m^2)	(10^3 m^2)	(10^4 m^3)	(10^4 m^3)		
Impact zone	13.59	1.83	1.06	15.42	0.73	0.81	1.59	0.90

371 2.3 Development of empirical vulnerability models for buildings

372 2.3.1 Damage class of buildings

373 Kule village encompasses a total of 128 buildings, with 36 buildings on the left bank
374 affected by postfire debris flows in the G1 gully. The damage to buildings notably depends on
375 their structural type, material resistance and distribution density (Zhang et al., 2018). In the
376 study area, 95% of the affected main building structures are BC structural-type buildings, which
377 are widely distributed in mountainous areas across China (Chen et al., 2021). We subsequently
378 aimed to develop vulnerability curves for BC buildings. Most buildings in the study area
379 comprise 1-3 floors, and the building height ranges from 3-8 m. To determine the degree of
380 damage to buildings caused by debris flows, it is necessary to establish a classification standard
381 on the basis of the actual structural and damage degree conditions (Hu et al., 2012; Lee et al.,
382 2024). Table 4 provides the four categories of damage to a given structure and the corresponding
383 vulnerability index values, including slight, moderate, extensive, and complete damage. On the
384 basis of the above assumptions and analysis, damaged buildings affected by debris flows in
385 Kule village were constructed (Appendix A).

386 Table 4 Damage classes and definitions for buildings (Hu et al., 2012; Wang et al., 2024; Lee
387 et al., 2024)

Damage class	Damage description	Value
Slight	Minor nonstructural damage occurred, with no impact on stability; damage was limited to furnishings and fittings.	0.1~0.3
Moderate	Cracks appeared in the wall, but stability remained unaffected; repairs are not urgent.	0.3~0.6

Extensive	The structure is partly destroyed, with partial loss of external and internal walls; evacuation is necessary; and reconstruction of damaged parts is required.	0.6~0.8
Complete	The structure is completely destroyed; evacuation is imperative; and complete reconstruction is necessary.	0.8~1.0

388 **2.3.2 Debris flow intensity**

389 In this study, six commonly used debris flow intensities were selected as multidimensional
 390 indicators of the destruction potential (Quan Luna et al., 2011; Eidsvig et al., 2014; Kang and
 391 Kim, 2016; Zhang et al., 2018; Chen et al., 2021; Wang et al., 2024; Lee et al., 2024), including
 392 the flow depth (h), flow velocity (v), impact pressure (p), momentum flux (f), overturning
 393 moment (m), and relative burial height (b).

394 The flow impact pressure includes both hydrostatic and hydrodynamic forces (Kang and
 395 Kim, 2016; Wang et al., 2024), and the total impact pressure exerted by a debris flow can be
 396 expressed as:

397
$$p = \frac{1}{2} \rho gh + \rho v^2 \tag{11}$$

398 where p is the impact pressure (Pa); v is the flow velocity (m/s); and h is the flow depth
 399 (m), ρ is the debris flow density (kg/m³).

400 The momentum flux can be obtained by multiplying the flow depth and the square of the
 401 flow velocity (Jakob et al., 2012; Chen et al., 2021):

402
$$f = hv^2 \tag{12}$$

403 where f is the momentum flux (m³/s²).

404 The overturning moment of a debris flow is related to the maximum flow velocity and

405 depth at which it collides with a given structure, as reported by Zhang et al. (2018):

$$406 \quad m = vh \quad (13)$$

407 where m is the overturning moment (m^2/s).

408 The relative burial height is defined by the deposition height and the affected building
409 height to represent the degree of burial damage (Totschnig et al., 2011; Zhang et al., 2018):

$$410 \quad b = \frac{h_d}{h_b} \quad (14)$$

411 where b is the relative burial height, h_d is the deposition height (m), and h_b is the building
412 height (m).

413 Under the same damage state, vulnerability values derived from different intensity
414 indicators may vary, potentially leading to inconsistent damage classification (Luo et al., 2023).
415 To enable a direct comparison of indicator performance in Discussion Section 4.1 (note that
416 normalized values are used exclusively for the analysis in that section), both intensity and
417 vulnerability values were normalized using the following equations (Zhang et al., 2024):

$$418 \quad I^* = \frac{I - \min(I)}{\max(I) - \min(I)} \quad (15a)$$

$$419 \quad V^* = \frac{V - \min(V)}{\max(V) - \min(V)} \quad (15b)$$

420 where I^* and V^* are the normalized values of the debris flow intensity and vulnerability,
421 respectively.

422 2.3.3 Vulnerability curve

423 The vulnerability model captures the relationship between the probability of building
424 damage reaching a certain state and the debris flow intensity (Cui et al., 2011). Notably,

425 postdisaster data-driven vulnerability curves can be expressed via function models (Fuchs et al.,
 426 2019). Currently, many vulnerability functions, such as logistic, Weibull, exponential, power-
 427 law and Avrami functions, are employed (Quan Luna et al., 2011; Eidsvig et al., 2014; Chen et
 428 al., 2021; Lee et al., 2024). However, the uncertainties in these models originate from the curve
 429 fitting process. For example, the use of the exponential function cannot guarantee that the curve
 430 passes through the origin. Therefore, recent studies have indicated that [lognormal cumulative](#)
 431 [distribution function \(LNCDF\)](#)~~LNCDF-based~~ vulnerability curves provide better performance
 432 (Luo et al., 2023):

$$433 \quad V = \Phi \left[\frac{1}{\beta} \ln \left(\frac{I}{I_m} \right) \right] \quad (16)$$

434 where β is the standard deviation of the logarithm of the hazard intensity; I is the debris
 435 flow hazard intensity; I_m is the median hazard intensity; [V is vulnerability value \(0-1\)](#); and Φ is
 436 the LNCDF, which can be expressed as follows:

$$437 \quad \Phi(x) = \int_0^x \frac{1}{\sqrt{2\pi}\sigma t} e^{-\frac{(\ln(t)-\mu)^2}{2\sigma^2}} dt \quad (17)$$

438 where μ is the mean of the LNCDF, and σ is the standard deviation of the LNCDF.

439 [The performance of models was comparatively analysed via four dimensionless](#)
 440 [performance indices, namely, the coefficient of determination \(\$R^2\$ \), the mean relative error](#)
 441 [\(MRE\), the Theil inequality coefficient \(TIC\), and the prediction accuracy factor \(PAF\).](#)
 442 [Notably, lower MRE and TIC values reflect higher model performance. Additionally, the closer](#)
 443 [the PAF value is to 1, the better the agreement between the calculated and experimental values](#)
 444 [\(the higher the prediction accuracy\). These indices can be calculated as follows \(Lee et al., 2024;](#)

445 [Wang et al., 2018](#)):

$$446 \quad R^2 = 1 - \frac{\sum_{i=1}^N (I_{cal,i} - I_{obs,i})^2}{\sum_{i=1}^N (I_{cal,i} - \bar{I}_{obs,i})^2} \quad (18)$$

$$447 \quad MRE = \frac{1}{N} \sum_{i=1}^N \frac{|I_{cal,i} - I_{obs,i}|}{I_{obs,i}} \quad (19)$$

$$448 \quad TIC = \frac{\sqrt{\left(\sum_{i=1}^N (I_{cal,i} - I_{obs,i})^2\right) / N}}{\sqrt{\left(\sum_{i=1}^N I_{cal,i}^2\right) / N} + \sqrt{\left(\sum_{i=1}^N I_{obs,i}^2\right) / N}} \quad (20)$$

$$449 \quad PAF = 10^{\frac{\sum_{i=1}^N \log|I_{cal,i} / I_{obs,i}|}{N}} \quad (21)$$

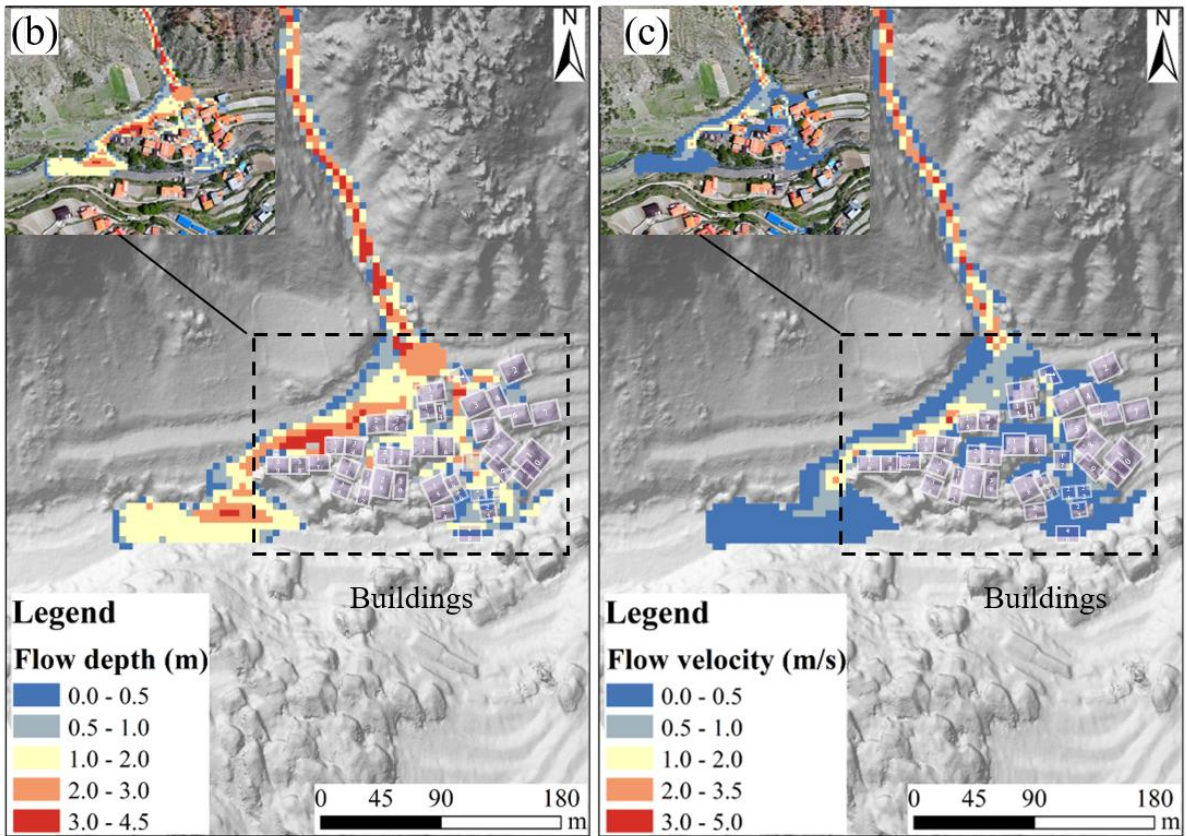
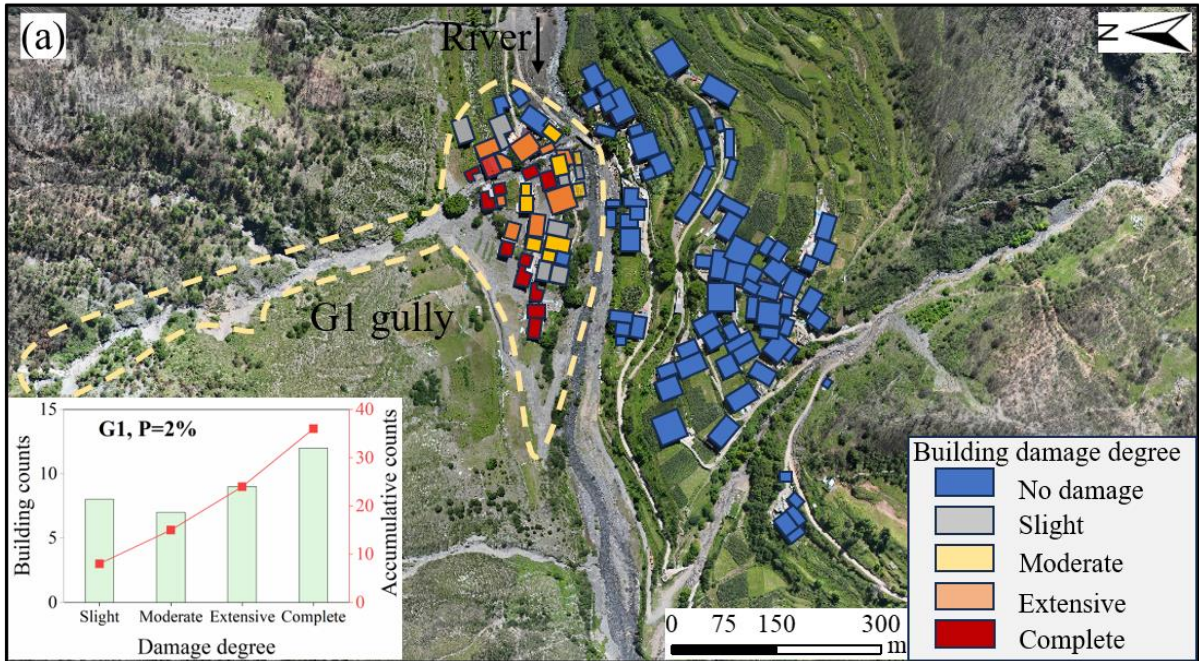
450 [where \$N\$ is the total number of data points, and \$I_{cal,i}\$ and \$I_{obs,i}\$ are the calculated and observed](#)
451 [values of case \$i\$, respectively.](#)

452 **3. Results**

453 **3.1 Reproduction of the debris flow intensity and building damage in the G1 gully**

454 Fig. 7a shows the characteristics of the degree of damage to buildings and the distribution
455 of buildings in the G1 gully. There are 36 buildings on the left bank of Kule village affected by
456 postfire debris flows in the G1 gully. Notably, the numbers of buildings with slight, moderate,
457 extensive and complete damage are 8, 7, 9 and 12, respectively. Fig. 7b shows that the FLO-2D
458 simulations reproduce the runout process of debris flows in the G1 gully that occurred on 10
459 May 2024, and distribution maps of the inundation area, flow velocity and flow depth were
460 obtained. The buildings were impacted and buried by debris flows, the flow depth near the
461 impacted buildings ranged from 0.25 to 2.61 m, and the flow velocity near the buildings ranged
462 from 0.04 to 1.93 m/s. This occurred because the debris flow energy partly dissipates under the

463 influence of building groups, and sediment is deposited inside the buildings. The debris flow
 464 also partially entered the main river, causing blockages at bridges connecting the villages on
 465 both sides (Fig. 7c).

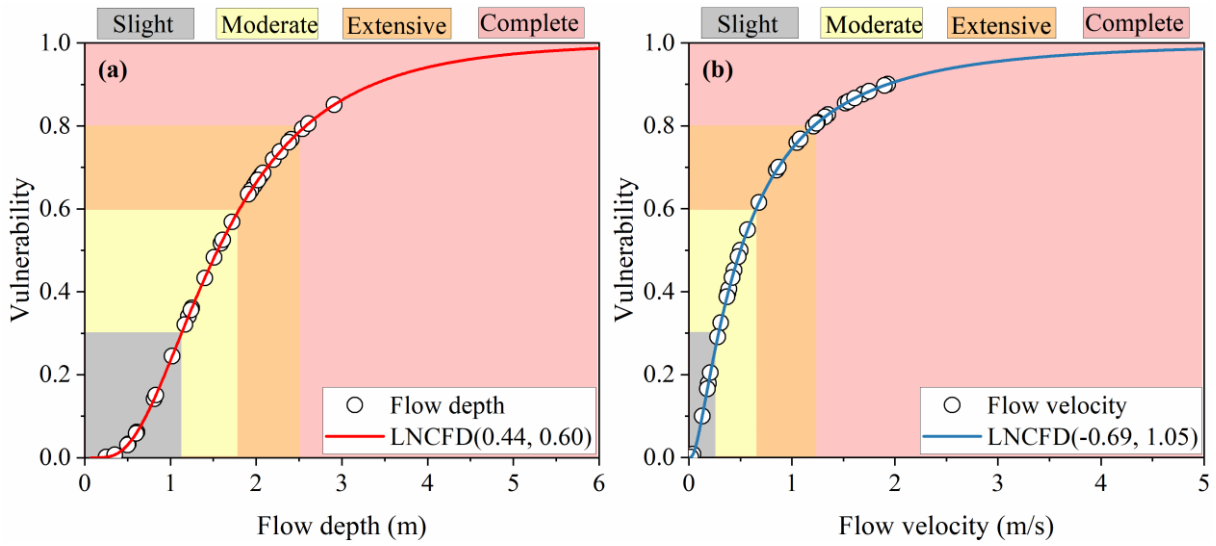


466

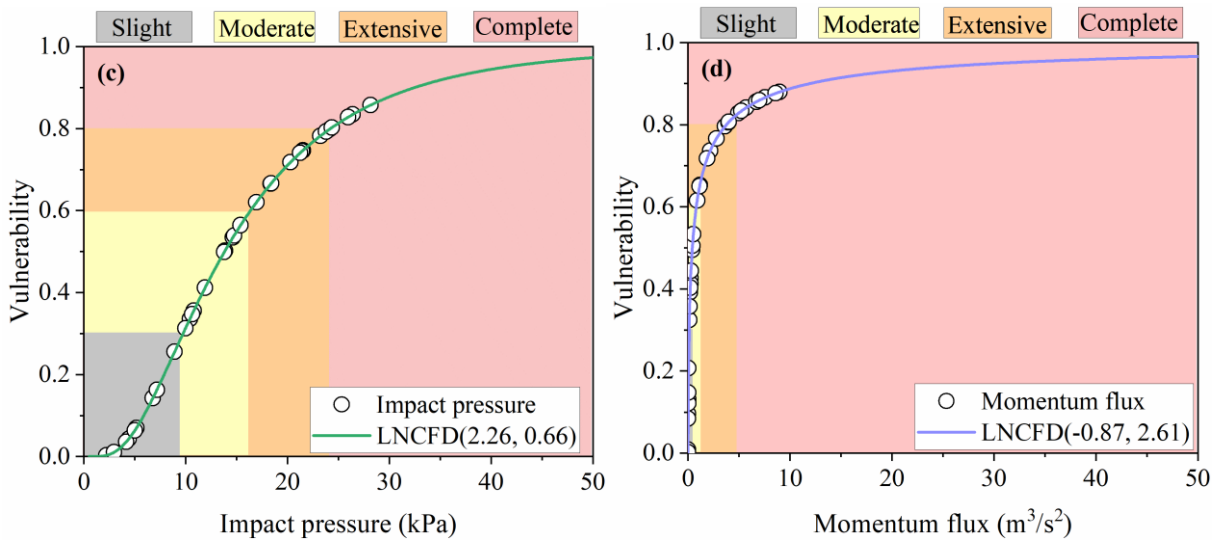
467 [Figure 7. Building damage from field survey and debris flow reconstruction using FLO-2D in](#)
468 [the G1 gully: \(a\) Distribution and statistics of building damage; \(b\) flow depth map; \(c\) flow](#)
469 [velocity map.](#)

470 **3.2 [Development of the vulnerability model](#) ~~Construction of the vulnerability model~~**

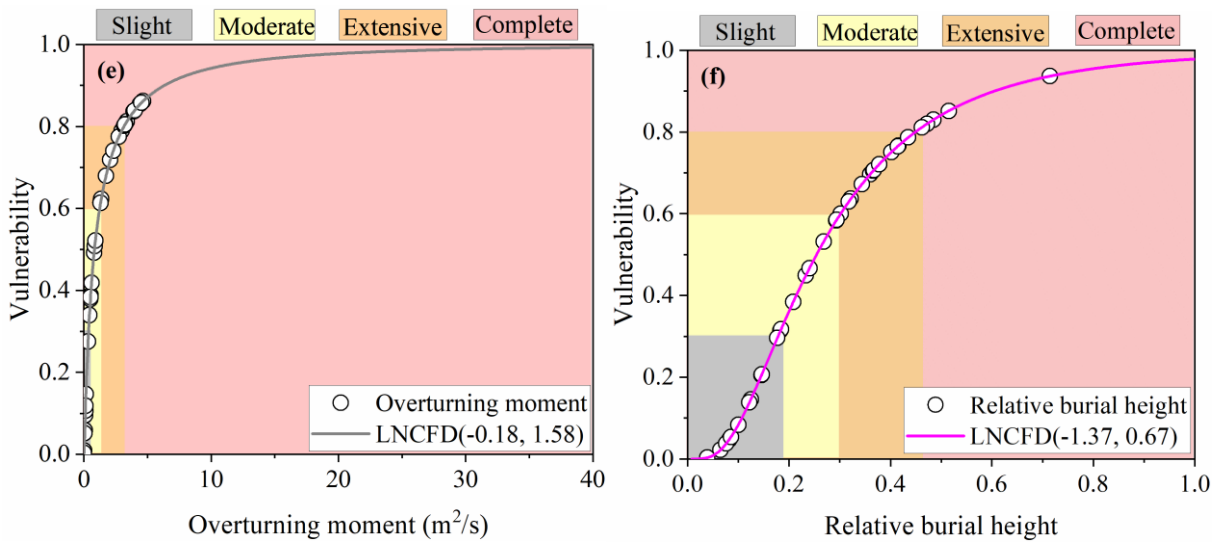
471 Fig. 8 shows six groups of developed vulnerability curves for the 2024 postfire debris flow
472 events in the G1 gully, including the flow depth, flow velocity, impact pressure, momentum
473 flux, overturning moment and relative burial height. The vulnerability curve can be obtained
474 via a continuum function relating the debris flow intensity (X-axis) to the degree of building
475 damage (Y-axis). The LNCDF effectively described the trend in the data. Each vulnerability
476 curve is a monotonically increasing function, indicating that with increasing debris flow
477 intensity, the probability of failure gradually increases. When the slope of the vulnerability
478 curve suddenly increases, the ability of the structure to resist disasters rapidly decreases after
479 critical-strength debris flow disaster occurrence, leading to a rapid increase in the probability
480 of failure. Specifically, to reach a maximum vulnerability value of 1, BC buildings necessitate
481 a flow depth greater than 6 m, a flow velocity of 5 m/s, an impact pressure of 50 kPa, a
482 momentum flux of $50 \text{ m}^3/\text{s}^2$, and an overturning moment of $40 \text{ m}^2/\text{s}$. However, completely
483 damaged buildings (with a vulnerability value exceeding 0.8) can no longer function properly.
484 Thus, the critical value of failure is lower, corresponding to a flow depth of 2.5 m, a flow
485 velocity of 1.3 m/s, an impact pressure of 25 kPa and a relative burial height of 0.48.
486 Additionally, the responses of the various indicators to vulnerability differed, and these
487 differences are analysed in greater detail in the subsequent chapter.



488



489



490

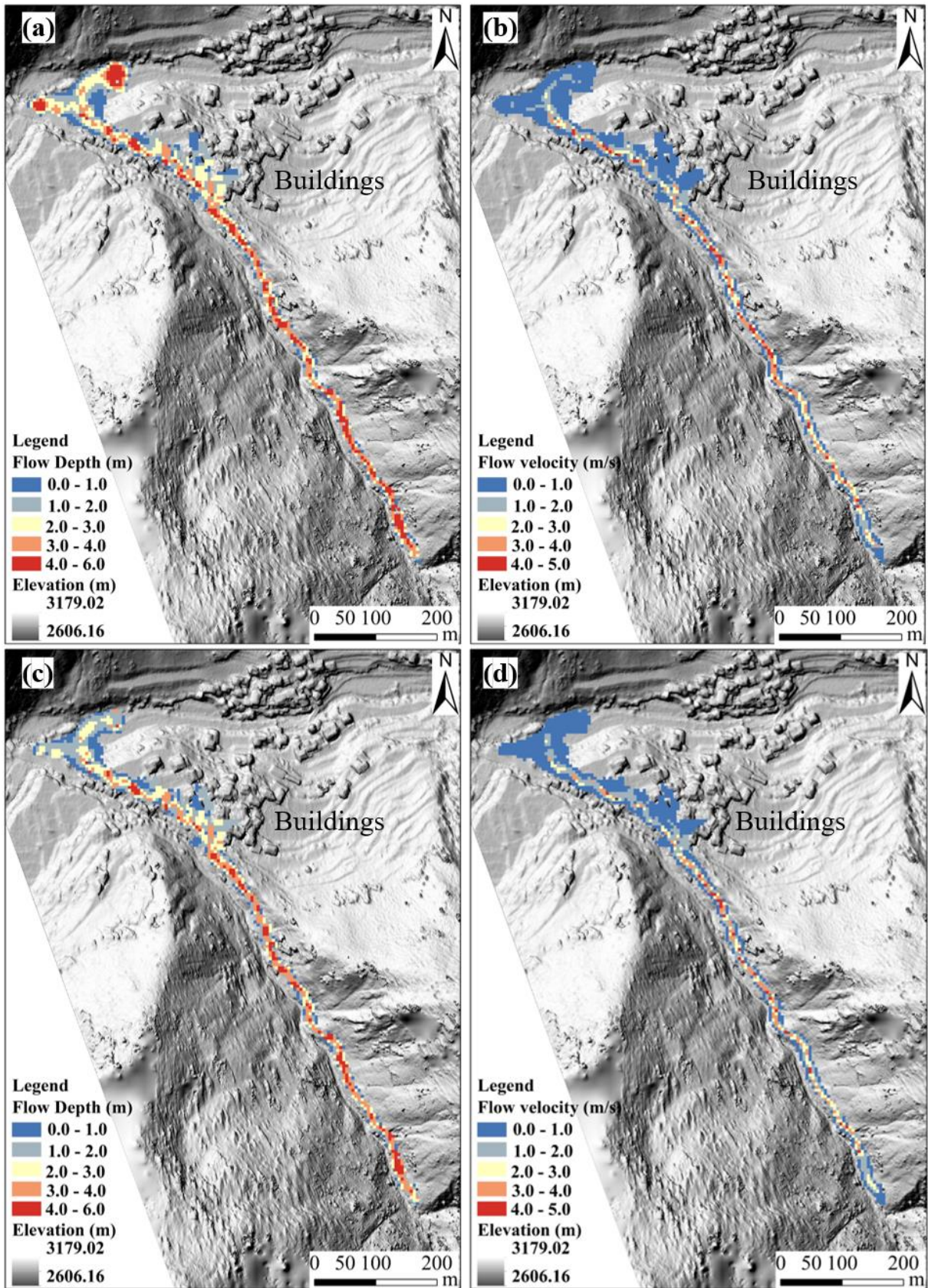
491 Figure 8. Vulnerability curves for debris flow intensities: (a) Flow depth, (b) flow velocity, (c)

492 impact pressure, (d) momentum flux, (e) overturning moment, and (f) relative burial height.

493 **3.3 Application of the vulnerability model in the G2 gully**~~Prediction of the debris flow~~
494 ~~intensity and application of the damaged building vulnerability model in the G2 gully~~

495 Potential postfire debris flow events may occur in the G2 gully, thus posing a serious threat
496 to buildings on the right bank of Kule village. Fig. 9 shows the prediction of potential debris
497 flows in the G2 gully using the FLO-2D model under reproduction frequency conditions of P=2%
498 (the peak flow is 40 m³/s) and P=1% (the peak flow is 48 m³/s). The simulated scenarios
499 revealed that the buildings near the channel were significantly affected by the debris flow, and
500 the debris flow flowed into the main river, causing deposition and blockage. The maximum
501 flow depth and flow velocity around the buildings are 3.50 m and 2.36 m/s, respectively. A
502 comparison of the flow depths between the two recurrence periods revealed that the maximum
503 value under P=1% surpassed that under P=2 by 20%.

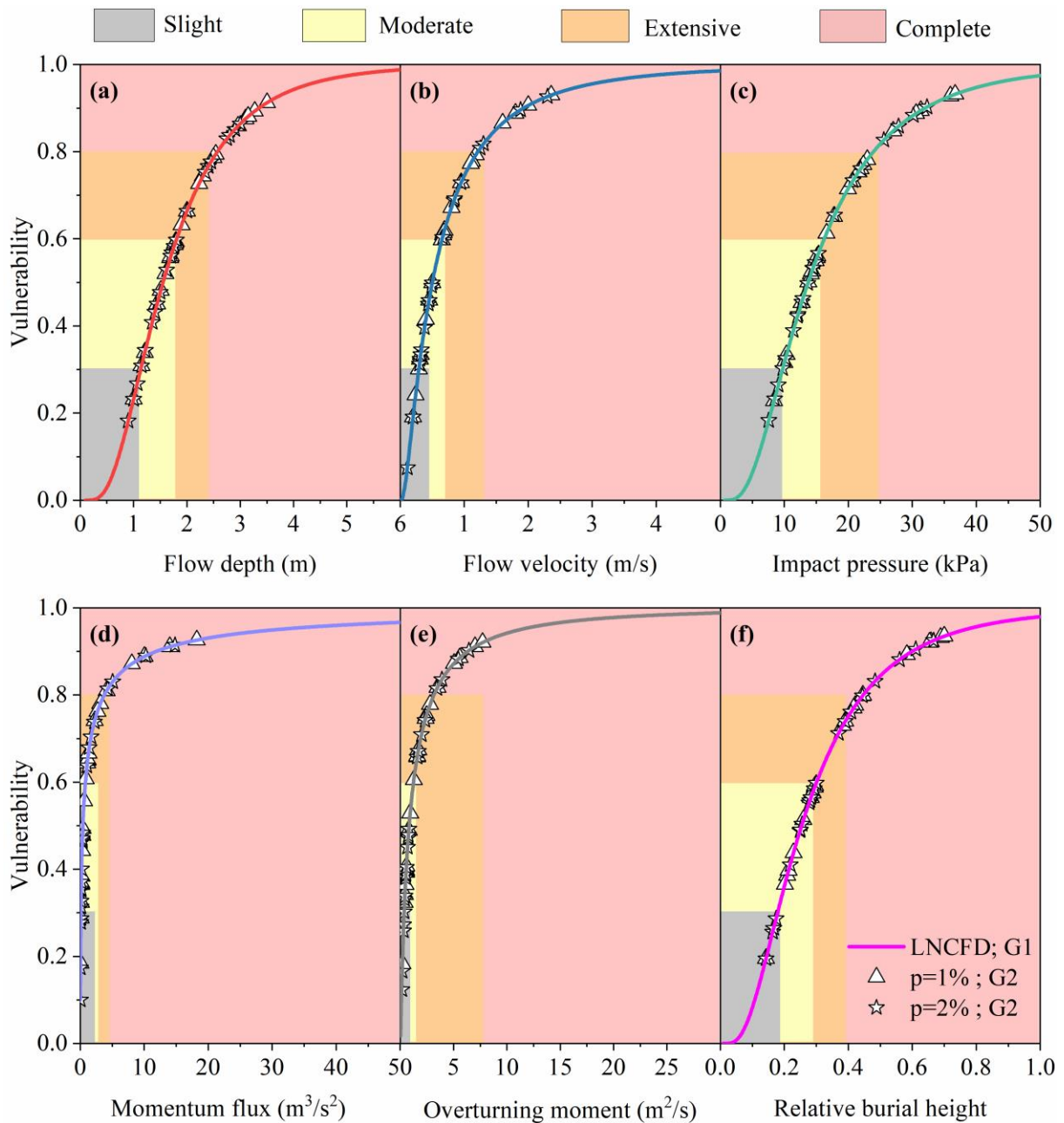
504 Then, by applying the established vulnerability model to the debris flow intensity data of
505 the G2 gully (Fig. 10), the vulnerability value of damaged buildings in the G2 gully can be
506 calculated from the generated curves (Appendix B). Next, four categories were determined
507 through a combination of vulnerability values and the damage classification system. Fig. 11
508 shows the predicted building damage degree and the spatial distribution under different
509 recurrence periods. The predicted total number of affected buildings is 24, and the numbers of
510 buildings with slight, moderate, extensive and complete damage are 4, 12, 4 and 4, respectively,
511 for P=2%. Concurrently, the numbers of buildings with extensive and complete damage exhibit
512 a corresponding uptick under longer recurrence periods (Fig. 12).



513

514 Figure 9. Prediction of the potential debris flow in the G2 gully using the FLO-2D model: (a)

515 Flow depth, P=2%; (b) flow velocity, P=2%; (c) flow depth, P=1%; (d) flow velocity, P=2%.



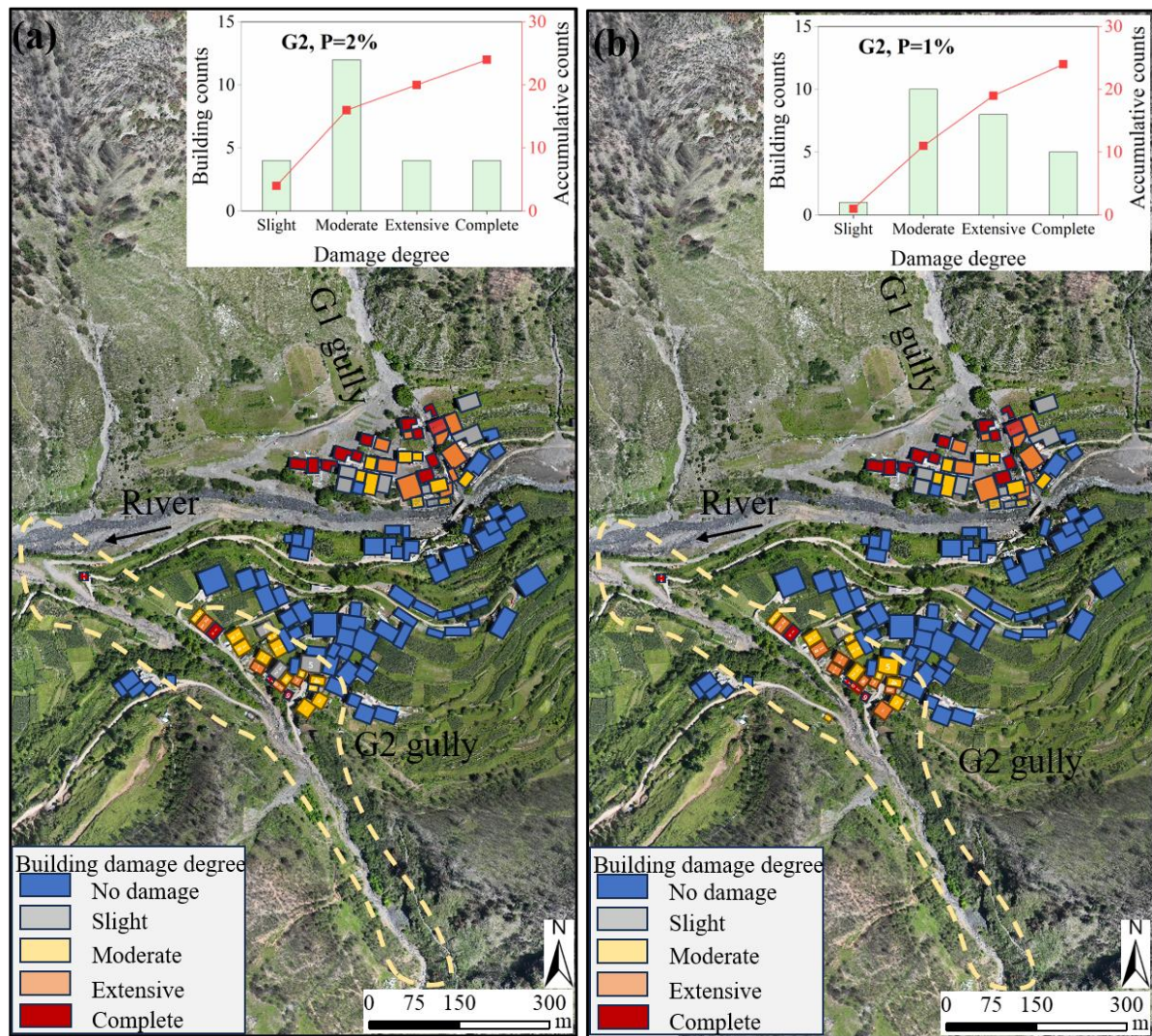
516

517 Figure 10. Vulnerability curves for different intensities of debris flows in the G2 gully according

518 to the established vulnerability model for determining the building damage status: (a) Flow

519 depth, (b) flow velocity, (c) impact pressure, (d) momentum flux, (e) overturning moment, and

520 (f) relative burial height.



521
 522 Figure 11. Predicted building counts with degree of damage and the spatial distribution in the
 523 G2 gully under different recurrence periods: (a) P=1%; (b) P=2%.

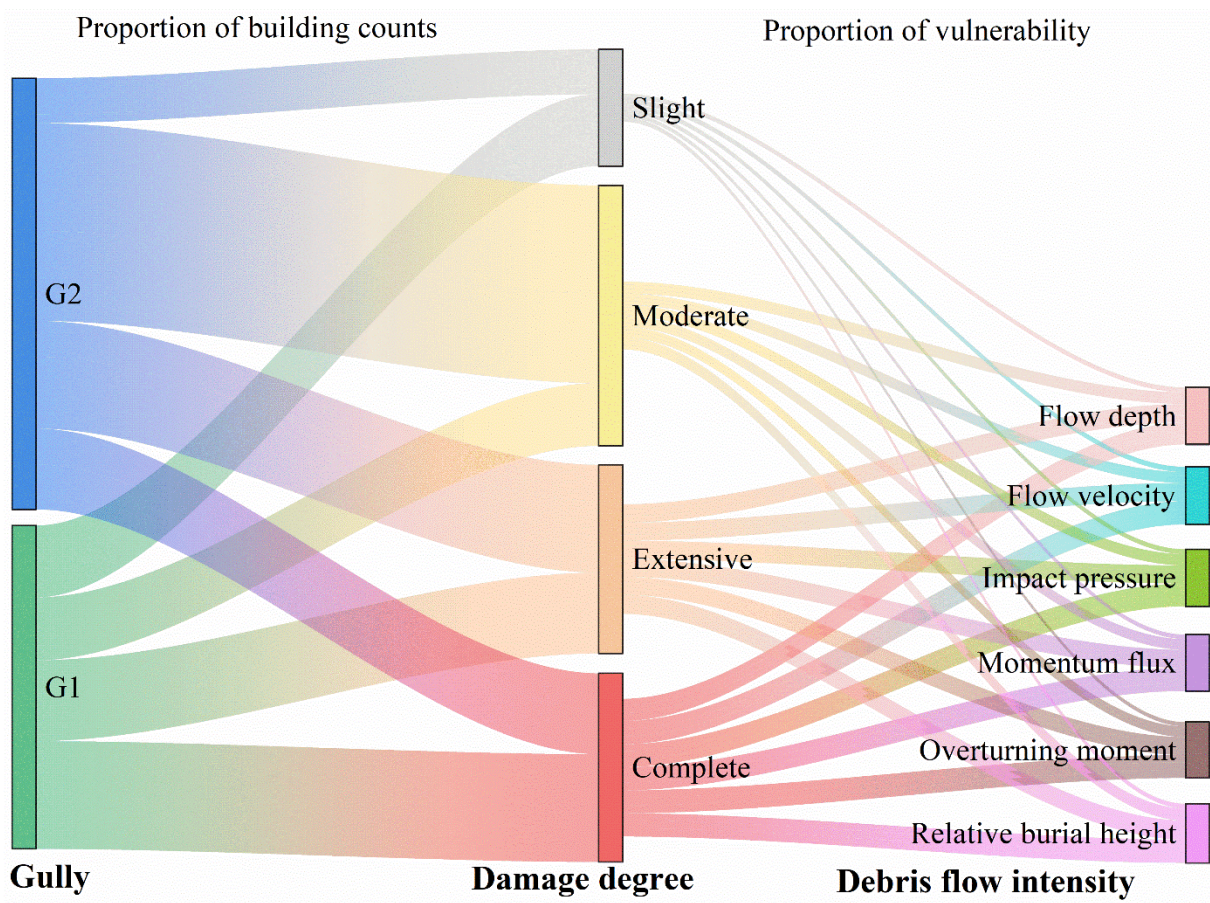
524 **4. Discussion**

525 **4.1 Comparison of building vulnerability models**

526 **5.1.1 Comparison of debris flow intensity indicators**

527 Firstly, we compared different debris flow intensity indicators. As mentioned earlier, we
 528 selected six indicators of the debris flow intensity to construct a building vulnerability model,
 529 but the vulnerability values also varied among the different indicators. Fig. 12 shows the

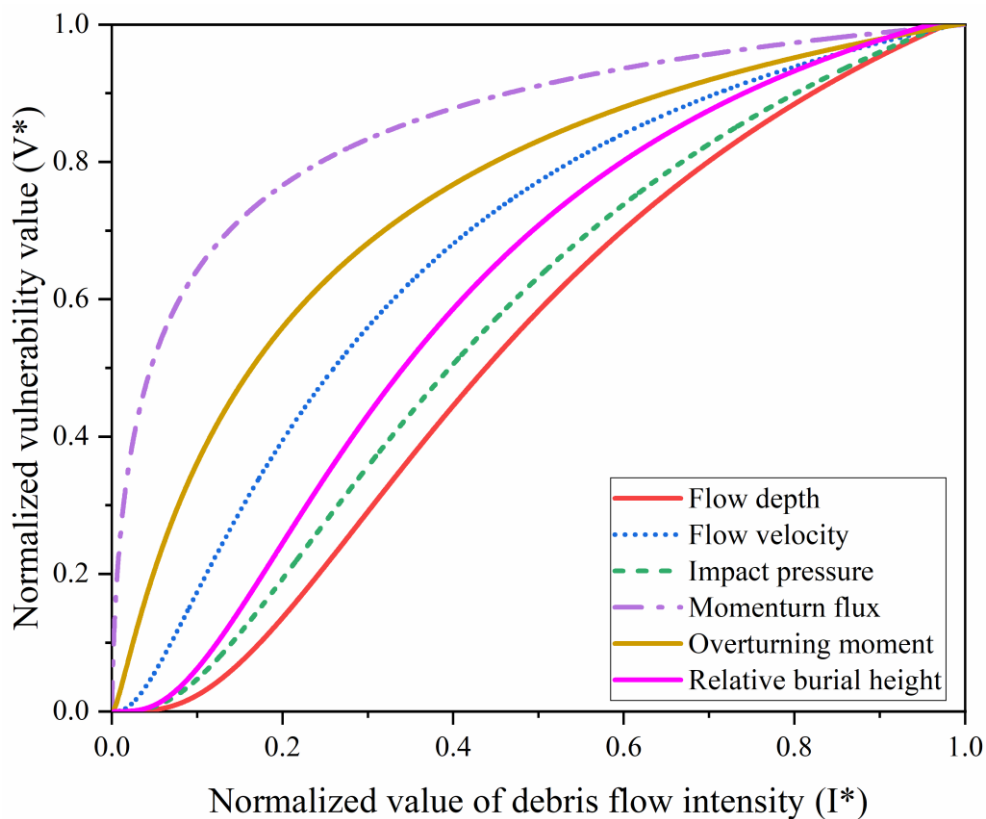
530 statistics of the total number of buildings and the vulnerability value under six debris flow
 531 intensities and four damage degrees in the G1 and G2 gullies of Kule village. The line width
 532 indicates the number of damaged buildings and their vulnerability value, with a thicker line
 533 indicating a higher value. The buildings in Kule village mainly exhibited moderate and
 534 complete damage.



535
 536 Figure 12. Statistics on the number of buildings and vulnerability under different debris flow
 537 intensities and damage degrees in the G1 and G2 gullies of Kule village.

538 The differences and sensitivities of the six curves in evaluating the vulnerability of
 539 damaged buildings are compared (Fig. 13). In terms of the properties of the normalized LNCDF
 540 curves, the larger the mean (μ) value is, the more the curve shifts to the right, indicating an
 541 increased probability of I^* attaining a larger value. The higher the standard deviation (σ) is, the

542 flatter the curve and the more dispersed the probability distribution. Conversely, the lower σ ,
543 the steeper the curve is, indicating a narrower range of I^* values and a more concentrated
544 probability distribution. As shown in Fig. 13, the momentum flux and overturning moment
545 curves are steeper, indicating higher sensitivity of these indicators accompanied by a rapid
546 increase in the probability of failure and more effective determination of the boundaries of the
547 different damage categories (Barnhart et al., 2024). Additionally, the flow depth and impact
548 pressure curves are relatively gradual, with low sensitivity, but the stability and accuracy of
549 determining the degree of damage are greater (Wang et al., 2024; Lee et al., 2024). Furthermore,
550 the impact pressure provides a more intuitive physical interpretation, indicating the
551 destructiveness of debris flows in relation to both the hydrostatic pressure and dynamic
552 overpressure, which has facilitated its widespread adoption in disaster risk assessment (Quan
553 Luna et al. 2011; Wang et al., 2024).



554

555 Figure 13. Comparison of vulnerability curves of the normalized debris flow intensity.

556 ~~5.1.2 Comparison of the proposed vulnerability models for brick-concrete buildings~~

557 Secondly, we compared the proposed vulnerability model. Table 5 shows a comparison
558 between the proposed vulnerability models for BC buildings and models established in previous
559 studies (Quan Luna et al. 2011; Eidsvig et al. 2014; Kang and Kim, 2016; Zhang et al., 2018;
560 Chen et al., 2021; Wang et al., 2024; Lee et al., 2024). ~~Specifically, Quan Luna et al. (2011)~~
561 ~~proposed two vulnerability curves for 13 unreinforced buildings in Valtellina Valley, Northern~~
562 ~~Italy. Eidsvig et al. (2014) established vulnerability curves for 53 buildings affected by debris~~
563 ~~flows in Martell Valley, South Tyrol, Italy. Kang and Kim (2016) proposed three vulnerability~~
564 ~~curves using data from 16 damaged buildings and 11 debris flows that occurred in Korea. Zhang~~
565 ~~et al. (2018) developed six vulnerability curves to assess damage to BC buildings caused by~~
566 ~~debris flows in Zhouqu County, northwestern China. Chen et al. (2021) constructed a physical~~
567 ~~fragility curve for 19 BC buildings damaged by debris flows that occurred in the Cutou Gully,~~
568 ~~Wenchuan County, China. Wang et al. (2024) developed two vulnerability curves for 41~~
569 ~~damaged buildings in the Wangzhuangwu watershed, Zhejiang Province, eastern China.~~ Fig. 14
570 shows a comparison of the proposed vulnerability curves for different debris flow intensities.
571 For flow depth (Fig. 14a), our curve aligns closely with Quan Luna et al. (2011) and Zhang et
572 al. (2018), while falling between the curves of Wang et al. (2024) and Kang and Kim (2016).
573 The complete damage threshold ($V=0.8$) occurs at 2.5 m in this study, compared to 1.3 m in
574 Wang et al. (2024). For flow velocity (Fig. 14b), our curve exhibits a steeper slope than those
575 of Zhang et al. (2018) and Kang and Kim (2016). The impact pressure curve (Fig. 14c) shows

576 an initially steep slope similar to Zhang et al. (2018), then flattens as it approaches complete
577 damage, reaching 25 kPa at $V=0.8$. This value is lower than the 30 kPa reported by Quan Luna
578 et al. (2011), Kang and Kim (2016), and Lee et al. (2024). For momentum flux (Fig. 14d), our
579 curve resembles that of Chen et al. (2021) but lies well below Zhang et al. (2018). Complete
580 damage ($V=1.0$) occurs at $90 \text{ m}^3/\text{s}^2$ in this study, compared to $131 \text{ m}^3/\text{s}^2$ in Zhang et al. (2018).
581 The overturning moment curve (Fig. 14e) is steeper than that of Zhang et al. (2018), reaching
582 $V=0.8$ at $4.0 \text{ m}^2/\text{s}$ compared to $20.1 \text{ m}^2/\text{s}$. For relative burial height (Fig. 14f), our curve is
583 considerably steeper than Zhang et al. (2018).

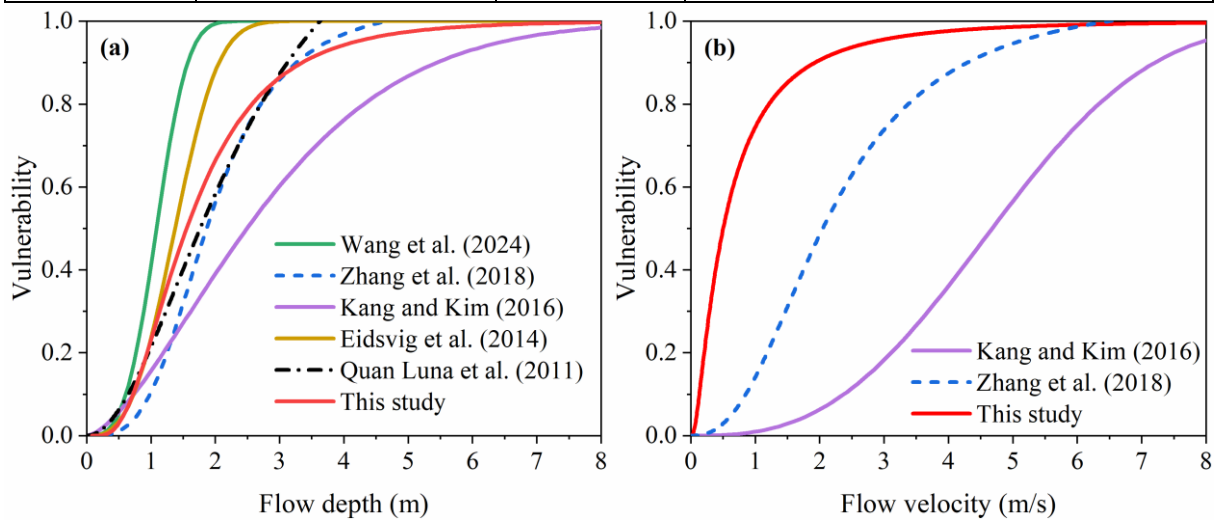
584 The observed differences between our vulnerability curves and those established in
585 previous studies may be attributed to a combination of factors. At a general level, variations in
586 regional building codes, construction practices, building geometry, and debris flow
587 characteristics (e.g., volume, density, event scale) across study areas can influence vulnerability
588 thresholds (Kang and Kim, 2016; Zhang et al., 2018). However, the distinct nature of postfire
589 debris flows in this study likely plays a more important role. Wildfires alter watershed
590 conditions in ways that increase the complexity and variability of debris flow processes. First,
591 fire increases the proportion of loose, fine particles in surface soil (Ouyang et al., 2023), which
592 are easily entrained and lead to higher solid concentrations and a greater tendency for deposition
593 and building inundation. This may explain the higher complete damage thresholds observed for
594 flow depth and relative burial height. Second, fire-damaged root systems and reduced slope
595 infiltration capacity result in more pronounced sheet erosion and numerous small runoffs after
596 rainfall, subjecting buildings to multi-directional and uneven impacts. Burned basins also

597 exhibit lowered rainfall thresholds for debris flow initiation, leading to higher event frequency
598 over extended periods (Fraser et al., 2022; Ouyang et al., 2023). These factors likely contribute
599 to the steeper slopes of our flow velocity and overturning moment curves. Third, high
600 temperatures from fire can weaken building envelopes, lowering their initial resistance to
601 dynamic impact. This may explain the lower impact pressure (25 kPa) required to reach V=0.8
602 and the lower momentum flux threshold (90 m³/s²) for complete damage compared to non-
603 postfire settings. Collectively, these postfire-specific mechanisms introduce greater variability
604 into intensity-damage relationships and explain the deviations between our curves and those
605 derived from non-postfire settings.

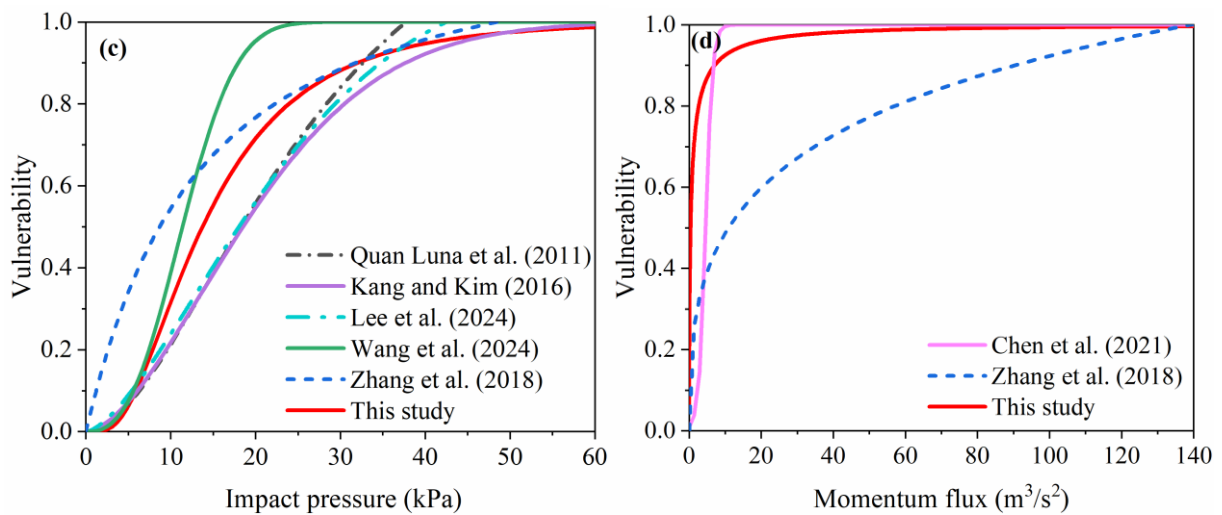
606 Table 5 Comparison of the vulnerability curves of brick-concrete buildings for different debris
607 flow intensities between this study and previous studies

Researchers	Debris flow density	Vulnerability functions	Vulnerability model for BC buildings
Quan Luna et al. (2011)	Flow depth, h Impact pressure, p	Logistic	$V = \frac{1.49 \times (h / 2.51)^{1.938}}{1 + (h / 2.51)^{1.938}}$ $V = \frac{1.59 \times (p / 28.16)^{1.808}}{1 + (p / 28.16)^{1.808}}$
Eidsvig et al. (2014)	Flow depth, h	Weibull distribution	$V = 1 - e^{-0.27h^{2.97}}$
Kang and Kim (2016)	Flow depth, h Flow velocity, v Impact pressure, p	Sigmoid, S-shaped	$V = 1 - e^{-0.170h^{1.537}}$ $V = 1 - e^{-0.009v^{2.775}}$ $V = 1 - e^{-0.005p^{1.690}}$
Zhang et al. (2018)	Flow depth, h Flow velocity, v Impact pressure, p Momentum flux, f Overturning moment, m Relative burial height, b	Logistic	$V = \frac{0.12 \times h^{3.39}}{1 + 9.24h^{3.39}} \quad V = \frac{0.17 \times v^{2.45}}{1 + 6.54 \times v^{2.45}}$ $V = \frac{0.08 \times p^{1.08}}{1 + 15.45p^{1.08}} \quad V = \frac{0.24 \times f^{0.40}}{1 + 10.23 \times f^{0.40}}$ $V = \frac{0.15 \times m^{1.15}}{1 + 7.83m^{1.15}} \quad V = \frac{1096 \times b^{1.54}}{1 + 0.0009b^{1.54}}$

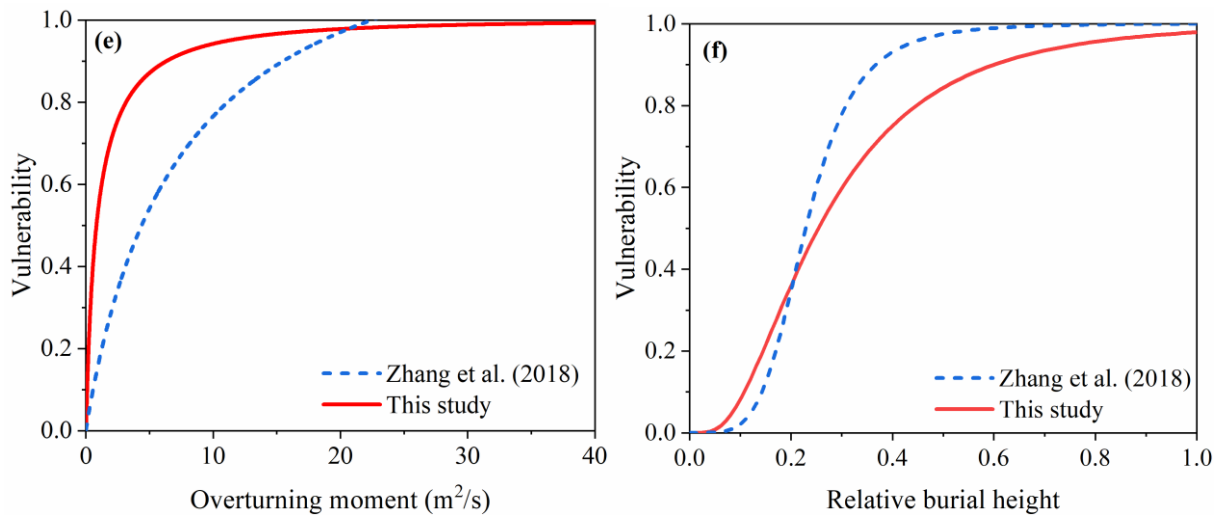
Chen et al. (2021)	Momentum flux, f	Exponential	$V = 1 / (1 + e^{-1.036f + 4.721})$
Wang et al. (2024)	Flow depth, h Impact pressure, p	Weibull distribution	$V = 1 - e^{-0.53h^{3.26}}$ $V = 1 - e^{-0.49(0.1p)^{2.65}}$
Lee et al. (2024)	Impact pressure, p	Avrami	$V = 1.129(1 - e^{-0.007 \times p^{1.530}})$
This study	Flow depth, h Flow velocity, v Impact pressure, p Momentum flux, f Overturning moment, m Relative burial height, b	Lognormal cumulative distribution function	$V = \Phi \left[\frac{1}{0.60} \ln \left(\frac{h}{e^{0.44}} \right) \right]$ $V = \Phi \left[\frac{1}{1.05} \ln \left(\frac{v}{e^{-0.69}} \right) \right]$ $V = \Phi \left[\frac{1}{0.66} \ln \left(\frac{p}{e^{2.26}} \right) \right]$ $V = \Phi \left[\frac{1}{2.61} \ln \left(\frac{f}{e^{-0.87}} \right) \right]$ $V = \Phi \left[\frac{1}{1.58} \ln \left(\frac{m}{e^{-0.18}} \right) \right]$ $V = \Phi \left[\frac{1}{0.67} \ln \left(\frac{b}{e^{-1.37}} \right) \right]$



608



609



610

611 Figure 14. Comparison of the vulnerability curves with previous models for different debris
 612 flow intensities.

613 **5.1.3 Comparison of vulnerability functions**

614 Finally, the differences between the various vulnerability curves also depend on the
 615 vulnerability function models employed. Table 6 provides the existing vulnerability function
 616 models, including [Logistic, Weibull, Exponential, LNCDF and Avrami functions](#) ~~logical~~
 617 ~~functions, Weibull functions, exponential functions, LNCDF models and Avrami functions~~
 618 (Quan Luna et al., 2011; Eidsvig et al., 2014; Kang and Kim, 2016; Zhang et al., 2018; Chen et
 619 al., 2021; Luo et al., 2023; Wang et al., 2024; Lee et al., 2024). We analysed the performance
 620 of the function models using data from this study and previous research (Fig. 15). The
 621 performance values of different function models were compared using the flow depth and
 622 impact pressure as examples (Fig. 15). The S-shaped function models (Logistical, Weibull,
 623 Avrami and LNCDF models) clearly performed better than the exponential function model did,
 624 whose vulnerability curve did not pass through the origin (Fig. 15a; b) and may be heavily
 625 affected by outliers. In addition, the coefficients of determination of all the function models did

626 not significantly differ, with R^2 values exceeding 0.88 (Table 6). This finding indicates that the
627 coefficient of determination only focuses on the degree of fit of the regression equation (Lee et
628 al., 2023), but it is not necessarily better for models with relatively large R^2 values, such as
629 exponential functions ($R^2=0.98$) with relatively large errors. The coefficient of determination is
630 affected by the complexity of the model, and overfitting may occur, which may lead to the
631 model performing well for training data but exhibiting a poor prediction ability with new data.
632 Therefore, the relative error and prediction accuracy of function models should be accounted
633 for (Wang et al., 2018).

634 In the comparison of the calculated and observed values, both the exponential and Avrami
635 functions clearly exhibited significant errors (Fig. 15c; d). Specifically, the MRE values for the
636 flow depth were 0.76 and 0.45, respectively, whereas the MRE values for the impact pressure
637 were 0.48 and 0.24, respectively (Table 6). However, the LNCDF model demonstrated the
638 highest statistical significance in terms of the relative error and accuracy, with MRE=0.16 and
639 PAF=1.15 for the flow depth and MRE=0.09 and PAF=1.09 for the impact pressure. In multiple
640 regression models, the coefficient of determination emphasizes the interpretability and fitting
641 performance, whereas the error prioritizes the prediction accuracy of the model. Overall, these
642 two metrics provide complementary insights for evaluating the overall performance of the
643 model. Overall, the performance of the various function models exhibited the following order:

644 LNCDF > logistic > Weibull > Avrami > exponential models. [LNCDF-based models are](#)
645 [insensitive to single data points because of the statistical parameter curve fitting process for](#)
646 [developing these models. It has been demonstrated that the LNCDF model can efficiently](#)

647 [increase the prediction performance, leading to a substantial reduction in output uncertainty,](#)
 648 [and this model is recommended for future applications \(Kean et al., 2019; Luo et al., 2023\).](#)

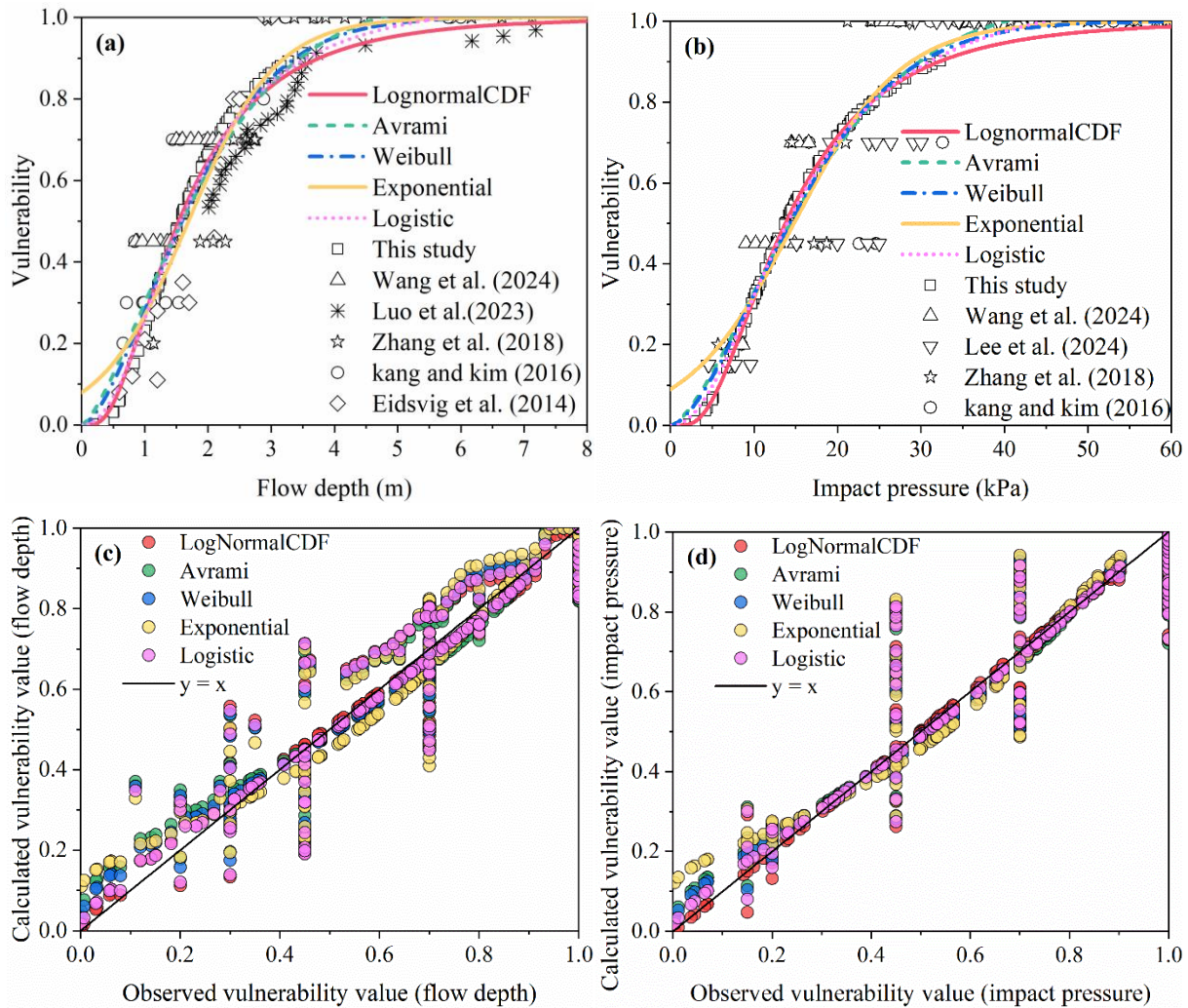


Figure 15. Performance comparison between different vulnerability function models: (a) Flow depth vulnerability models; (b) impact pressure vulnerability models; (c) observation and calculation values of the flow depth; (d) observation and calculation values of the impact pressure.

Table 6 Performance comparison between various data-driven building vulnerability function models

Research ers	Vulnerab ility	Function models	Flow depth				Impact pressure					
			R ²	MRE	TIC	PAF	R ²	MRE	TIC	PAF		

	models									
Quan Luna et al. (2011); Zhang et al. (2018)	Logistic	$V = \frac{a \times (\frac{x}{b})^c}{1 + (\frac{x}{b})^c}$	0.98	0.22	0.06	1.17	0.89	0.16	0.06	1.13
Chen et al. (2021)	Exponential	$V = \frac{1}{1 + e^{ax+b}}$	0.98	0.76	0.06	1.23	0.88	0.48	0.07	1.19
Eidsvig et al. (2014); Kang and Kim (2016); Wang et al. (2024)	Weibull	$V = 1 - e^{-(x/a)^b}$	0.88	0.37	0.06	1.20	0.89	0.22	0.06	1.15
Lee et al. (2024)	Avrami	$V = a(1 - e^{-bx^c})$	0.99	0.45	0.06	1.21	0.89	0.24	0.06	1.16
Luo et al. (2023); This study	LNCDF	$V = \Phi \left[\frac{1}{\beta} \ln \left(\frac{I}{I_m} \right) \right]$	0.88	0.16	0.06	1.15	0.88	0.09	0.06	1.09

657 Note: The parameters a, b, and c can be obtained directly by curve fitting.

658 4.2 Disaster reduction and emergency response suggestions

659 Both sides of Kule village are at risk of being impacted by the G1 and G2 gullies (Fig. 16).

660 Owing to the impact of wildfires, there is a large amount of loose material in these gullies,

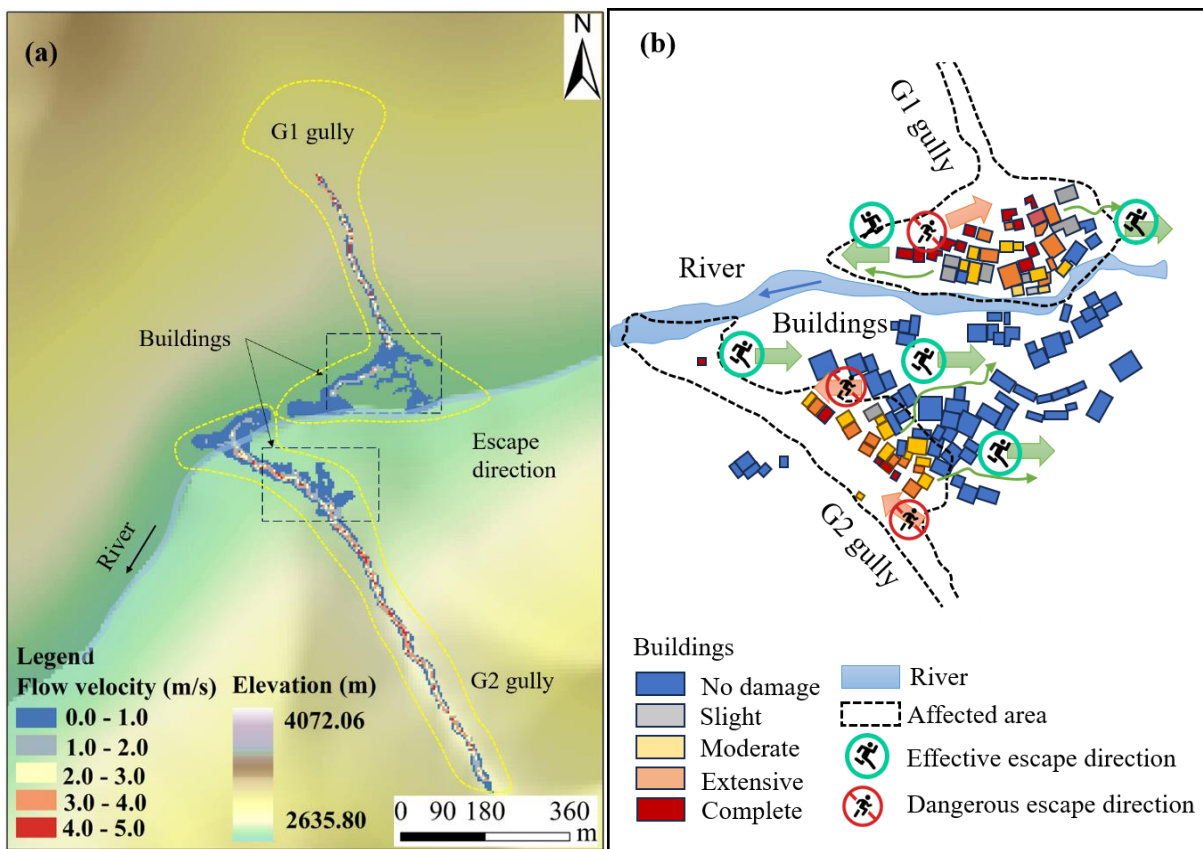
661 which can trigger postfire debris flows again under low rainfall thresholds. Through the above

662 field investigations and simulation predictions, debris flows can seriously damage buildings

663 downstream of the alluvial fan and even block the Kule River, posing a severe threat to the lives

664 of more than 300 people in the village. The most dangerous situation occurs when debris flows

665 occur in the two gullies simultaneously (Fig. 16a). An immediate emergency response is crucial,
 666 and the escape route should be oriented along the vertical direction of the debris flow channel
 667 for reaching a safe location in high terrain (Fig. 16b). Left-bank residents should evacuate from
 668 both sides, thereby avoiding crossing the river. In contrast, right-bank residents should evacuate
 669 swiftly from the high-terrain area on their side. The safest suggestion is for residents to leave
 670 the village under feasible conditions. In the long term, reforestation can stabilize soil and reduce
 671 sediment into channels (Yang et al., 2022; Vahedifard et al., 2024). Thus, restoring vegetation
 672 in burned areas is essential for effectively suppressing postfire debris flows and promoting local
 673 ecological recovery (Yang et al., 2024).



674
 675 Figure 16. Disaster prediction and emergency response suggestions: (a) Simulation of debris
 676 flows occurring simultaneously in the G1 and G2 gullies; (b) emergency response and risk

677 avoidance suggestions for the residents of Kule village.

678 4.3 Limitations and future work

679 Our results provide insights into assessing the vulnerability of buildings to debris flows
680 triggered by wildfires in Yajiang County. A combination of numerical simulation and function
681 model methods provided a distinct advantage in the development of vulnerability curves. The
682 spatial distributions of the flow depth and flow velocity can be visualized, and detailed physical
683 information can be obtained in a specific area (Zhang et al., 2018). Additionally, this study
684 highlights the importance of acknowledging and addressing the inherent uncertainty associated
685 with various debris flow intensity indicators and function models applied in vulnerability
686 assessments via a comparison of existing intensity indicators and evaluating the performance
687 of various function models. Notably, while the methodological framework combining field
688 investigation, numerical simulation, and vulnerability analysis is transferable to non-fire areas,
689 the specific vulnerability curve parameter values require recalibration when applied elsewhere.

690 However, several limitations should be acknowledged. First, during the numerical
691 modelling phase, terrain changes and sediment volume variations caused by debris flow
692 entrainment were neglected (Wang et al., 2024), and validation focused on depositional area
693 and runout volume, neglecting flow velocity along the path (Chen et al., 2021). Additionally,
694 due to limited understanding of postfire debris flow triggering and runoff mechanisms (Rengers
695 et al., 2016; Ouyang et al., 2023) and the introduction of burned wood into channels (Rengers
696 et al., 2023), only volume and peak flow were considered as recurrence period indicators (Cui
697 et al., 2018; Gorr et al., 2024), while other geological variables (e.g., particle size distribution,

698 viscosity, water content) were not incorporated (Chen et al., 2021). Second, differences in the
699 vulnerability curves of different indicators could cause uncertainty in vulnerability assessments
700 (Luo et al., 2023), where the percentage of buildings categorized may be inconsistent. The
701 slopes of the LNCDF-based curves increase slowly during the latter half, and intensity
702 calculations based on maximum values may lead to overestimation of ultimate failure strength
703 compared to actual values (Chen et al., 2021). Owing to the limited number of data points, to
704 increase the reliability of the vulnerability curves (Lee et al., 2024; Ettinger et al., 2016), more
705 data on postfire debris flow events and validations are needed in the future. Additionally,
706 transferring the G1-calibrated parameters to G2, an approach based on field observations of
707 comparable conditions between the adjacent catchments, introduces uncertainty as G2 is
708 potentially hazardous but has not yet experienced a debris flow. The G2 simulation results show
709 consistent orders of magnitude with similar regional events data (He et al., 2024). Direct
710 validation of G2 predictions warrants attention in future work. Finally, this study focused on
711 BC buildings, not accounting for other structural types (e.g., reinforced concrete frame
712 buildings), mechanical failure criteria for unreinforced masonry walls (Si et al., 2022), or
713 building-specific factors such as shape, orientation, number of floors, masking effects of
714 building complexes and construction codes (Lee et al., 2024; Wang et al., 2024). These
715 limitations emphasize the need for further research to enhance the comprehensive management
716 of hazard risks in mountainous rural areas.

717 Future research should focus on ensuring continuous, standardized post-event data
718 collection processes, which will enhance the practical applicability of the developed

719 vulnerability curves. Ultimately, this framework represents an important step towards
720 developing physical vulnerability models, thereby providing comprehensive insights into the
721 potential effects of future postfire debris flow events on buildings in similar regions and offering
722 valuable guidance for formulating disaster management and mitigation strategies.

723 **5. Conclusions**

724 This study ~~focused on assessing~~ assessed the vulnerability of buildings to postfire debris
725 flows in Kule village, Yajiang County. A physical vulnerability model for BC buildings was
726 established to support ~~the design of~~ effective disaster management and emergency evacuation
727 strategies for the region. The conclusions are as follows:

728 (1) Field investigations characterized postfire debris flow features in the G1 and G2 gullies
729 and documented damage to 36 BC buildings in Kule village. ~~A field investigation was conducted~~
730 ~~to analyse the characteristics of debris flows in the G1 and G2 gullies under the influence of~~
731 ~~wildfires and to document the damage features of 36 BC buildings in Kule village.~~ The volume
732 and peak discharge of postfire debris flows were calculated, and the damage degree of buildings
733 was categorized using a range of vulnerability indices.

734 (2) Dynamic runout processes were simulated using the FLO-2D numerical model, with
735 the reconstructed results calibrated to ensure consistency with actual situations. The simulations
736 captured the debris flow intensities, including the flow depth, flow velocity, impact pressure,
737 momentum flux, overturning moment, and relative burial height.

738 (3) Physical vulnerability curves for BC buildings damaged by postfire debris flows in the
739 G1 gully were developed. The vulnerability model was subsequently applied to the G2 gully,

740 ~~which may also experience postfire debris flows,~~ to predict potential building damage scenarios
741 and their spatial distributions. ~~Thus, emergency evacuation suggestions for Kule village were~~
742 ~~provided in the event of simultaneous debris flows in both gullies.,~~ enabling emergency
743 evacuation recommendations for Kule village in the event of simultaneous debris flows in both
744 gullies.

745 (4) Comparisons of ~~The~~ different vulnerability curves, intensity indicators, and function
746 models revealed that ~~were compared.~~ ~~Among the intensity indicators, the~~ momentum flux was
747 the most sensitive indicator for distinguishing damage categories, while ~~Conversely, the~~ impact
748 pressure could provide more accurate vulnerability values. Among the function models, the
749 LNCDF function model demonstrated the highest statistical performance (MRE=0.09,
750 PAF=1.09).

751 (5) The proposed vulnerability model exhibits certain limitations, emphasizing the
752 importance of acknowledging and addressing the inherent uncertainty associated with various
753 intensity indicators, function models, triggering and runoff mechanisms underlying postfire
754 debris flows, and building structure and orientation in future research.

755 ~~Future research should focus on ensuring continuous, standardized postevent data~~
756 ~~collection processes, which will enhance the practical applicability of the developed~~
757 ~~vulnerability curves. Ultimately, this framework represents an important step towards~~
758 ~~developing physical vulnerability models, thereby providing comprehensive insights into the~~
759 ~~potential effects of future postfire debris flow events on buildings in similar regions and offering~~
760 ~~valuable guidance for formulating disaster management and mitigation strategies.~~

762 **Author contributions**

763 **JW:** Writing - original draft, Methodology, Validation, Conceptualization. **JC:** Writing -
764 Review & editing, Supervision, Funding acquisition. **LZ:** Investigation, Data curation. **FY:**
765 Software. **XL:** Investigation. **WZ:** Resources. **HC:** Formal analysis.

766 **Declaration of competing interest**

767 The authors have no conflicts of interest to declare.

768 **Acknowledgements**

769 This study was supported by the National Key R&D Program of China (Grant No.
770 2024YFC3012705), the Nyingchi National Sustainable Development Experimental Zone
771 Project (2023-SYQ-007), the National Natural Science Foundation of China (Grant No.
772 41925030) and the Science and Technology Research Program of the Institute of Mountain
773 Hazards and Environment, Chinese Academy of Sciences (Grant No. IMHE-ZDRW-02).

774 **Data availability**

775 The authors agree to make data supporting the results or analyses presented in this paper
776 available upon reasonable request to the first author and corresponding author.

777

Appendix A Debris flow intensities and building damage degree in G1 gully

NO.	Flow depth (m)	Flow velocity (m/s)	Impact pressure (kPa)	Momentum flux (m^3/s^2)	Overturning moment (m^2/s)	Relative burial height	Damage degree
1	2.00	1.69	21.52	5.71	3.38	0.71	Complete
2	0.51	0.31	4.41	0.05	0.16	0.08	Slight
3	2.91	1.52	28.17	6.72	4.42	0.49	Complete
4	1.61	0.50	13.84	0.40	0.81	0.32	Extensive
5	1.98	1.05	18.37	2.18	2.08	0.36	Extensive
6	0.81	0.13	6.78	0.01	0.11	0.12	Slight
7	1.94	0.68	16.95	0.90	1.32	0.37	Extensive
8	1.61	0.85	14.64	1.16	1.37	0.27	Extensive
9	1.40	0.38	11.91	0.20	0.53	0.23	Moderate
10	2.20	1.35	21.42	4.01	2.97	0.29	Complete
11	1.51	0.87	13.87	1.14	1.31	0.30	Extensive
12	2.03	1.93	23.24	7.56	3.92	0.47	Complete
13	1.02	0.50	8.92	0.26	0.51	0.15	Moderate
14	1.21	0.44	10.41	0.23	0.53	0.18	Moderate
15	2.06	1.55	21.24	4.95	3.19	0.52	Complete
16	1.72	0.50	14.75	0.43	0.86	0.34	Extensive
17	2.08	1.32	20.29	3.62	2.75	0.42	Complete
18	0.61	0.19	5.14	0.02	0.12	0.12	Slight
19	1.25	0.48	10.80	0.29	0.60	0.21	Moderate
20	1.59	0.57	13.80	0.52	0.91	0.32	Extensive
21	0.83	0.39	7.17	0.13	0.32	0.18	Moderate
22	0.25	0.28	2.22	0.02	0.07	0.04	Slight
23	2.02	1.61	21.23	5.24	3.25	0.37	Complete
24	1.61	1.08	15.39	1.88	1.74	0.24	Extensive
25	1.24	0.42	10.63	0.22	0.52	0.18	Moderate
26	1.91	1.21	18.40	2.80	2.31	0.29	Extensive
27	1.17	0.37	9.98	0.16	0.43	0.15	Moderate
28	0.50	0.04	4.17	0.00	0.02	0.06	Slight
29	0.61	0.21	5.16	0.03	0.13	0.08	Slight
30	2.41	1.93	26.41	8.98	4.65	0.40	Complete
31	2.28	1.75	24.20	6.98	3.99	0.41	Complete
32	0.60	0.02	5.00	0.00	0.01	0.09	Slight
33	2.54	1.25	23.81	3.97	3.18	0.46	Complete
34	2.61	1.24	24.36	4.01	3.24	0.44	Complete
35	2.38	1.90	25.96	8.59	4.52	0.38	Complete
36	0.35	0.18	2.97	0.01	0.06	0.10	Slight

779 **Appendix B Debris flow intensities and predicted building counts in G2**

780 **gully: (a) Design frequency P=1%; (b) Design frequency P=12%**

781 (a) Design frequency P=1%

NO.	Flow depth (m)	Flow velocity (m/s)	Impact pressure (kPa)	Momentum flux (m ³ /s ²)	Overturning moment (m ² /s)	Relative burial height	Damage degree
1	2.30	0.69	19.97	1.10	1.59	0.38	Extensive
2	1.79	0.31	15.07	0.17	0.55	0.29	Moderate
3	1.90	0.67	16.59	0.85	1.27	0.42	Extensive
4	1.77	0.31	14.91	0.17	0.55	0.30	Moderate
5	1.15	0.50	10.00	0.29	0.58	0.21	Moderate
6	1.69	0.24	14.18	0.10	0.41	0.26	Moderate
7	2.54	0.67	21.92	1.14	1.70	0.39	Extensive
8	2.50	0.68	21.61	1.16	1.70	0.42	Extensive
9	3.50	2.00	35.96	14.00	7.00	0.58	Complete
10	3.10	1.80	31.33	10.04	5.58	0.69	Complete
11	2.96	1.18	27.02	4.12	3.49	0.66	Complete
12	1.60	0.50	13.75	0.40	0.80	0.21	Moderate
13	2.50	1.12	22.96	3.14	2.80	0.42	Extensive
14	2.00	0.80	17.75	1.28	1.60	0.44	Extensive
15	1.70	0.32	14.34	0.17	0.54	0.28	Moderate
16	1.51	0.29	12.72	0.13	0.44	0.23	Moderate
17	1.00	0.20	8.40	0.04	0.20	0.14	Slight
18	2.23	1.10	20.63	2.70	2.45	0.45	Extensive
19	1.44	0.65	12.71	0.61	0.94	0.29	Moderate
20	3.27	2.36	36.71	18.21	7.72	0.65	Complete
21	2.50	0.95	22.36	2.26	2.38	0.42	Extensive
22	1.78	0.45	15.17	0.36	0.80	0.30	Moderate
23	3.15	1.60	30.59	8.06	5.04	0.70	Complete
24	1.21	0.40	10.35	0.19	0.48	0.20	Moderate

782

783 (b) Design frequency P=2%

NO.	Flow depth (m)	Flow velocity (m/s)	Impact pressure (kPa)	Momentum flux (m ³ /s ²)	Overturning moment (m ² /s)	Relative burial height	Damage degree
1	1.70	0.44	14.49	0.33	0.75	0.28	Moderate
2	1.72	0.30	14.48	0.15	0.52	0.28	Moderate
3	1.35	0.31	11.41	0.13	0.42	0.30	Moderate
4	1.76	0.30	14.81	0.16	0.53	0.29	Moderate
5	0.90	0.20	7.57	0.04	0.18	0.16	Slight
6	1.62	0.33	13.68	0.18	0.53	0.25	Moderate
7	2.40	0.66	20.73	1.05	1.58	0.37	Extensive
8	1.80	0.45	15.34	0.36	0.81	0.30	Moderate
9	2.90	1.88	30.17	10.25	5.45	0.48	Complete
10	2.00	0.84	17.86	1.41	1.68	0.44	Extensive
11	2.75	1.25	25.56	4.30	3.44	0.61	Complete
12	1.07	0.30	9.07	0.10	0.32	0.14	Slight
13	2.45	0.95	21.94	2.21	2.33	0.41	Extensive
14	1.15	0.32	9.75	0.12	0.37	0.26	Moderate
15	1.50	0.38	12.74	0.22	0.57	0.25	Moderate
16	1.44	0.30	12.15	0.13	0.43	0.22	Moderate
17	1.22	0.11	10.18	0.01	0.13	0.17	Slight
18	1.50	0.50	12.92	0.38	0.75	0.30	Moderate
19	1.40	0.49	12.07	0.34	0.69	0.28	Moderate
20	2.80	2.30	32.32	14.81	6.44	0.56	Complete
21	2.34	0.85	20.72	1.69	1.99	0.39	Extensive
22	1.70	0.45	14.51	0.34	0.77	0.28	Moderate
23	3.00	1.30	27.86	5.07	3.90	0.67	Complete
24	1.00	0.30	8.48	0.09	0.30	0.17	Slight

784

785 **References**

- 786 Barnhart, K. R., Miller, C. R., Rengers, F. K., & Kean, J. W. (2024). Evaluation of debris-flow
787 building damage forecasts. *Natural Hazards and Earth System Sciences*, 24(4), 1459-1483.
788 <https://doi.org/10.5194/nhess-24-1459-2024>
- 789 Chang, M., Liu, Y., Zhou, C., & Che, H. (2020). Hazard assessment of a catastrophic mine
790 waste debris flow of Hou Gully, Shimian, China. *Engineering Geology*, 275, 105733.
791 <https://doi.org/10.1016/j.enggeo.2020.105733>
- 792 Chen, M., Tang, C., Zhang, X., Xiong, J., Chang, M., Shi, Q., ... & Li, M. (2021). Quantitative
793 assessment of physical fragility of buildings to the debris flow on 20 August 2019 in the
794 Cutou gully, Wenchuan, southwestern China. *Engineering Geology*, 293, 106319.
795 <https://doi.org/10.1016/j.enggeo.2021.106319>
- 796 Cui, P., Guo, X., Yan, Y., Li, Y., & Ge, Y. (2018). Real-time observation of an active debris flow
797 watershed in the Wenchuan Earthquake area. *Geomorphology*, 321, 153-166.
798 <https://doi.org/10.1016/j.geomorph.2018.08.024>
- 799 Cui, P., Hu, K., Zhuang, J., Yang, Y., & Zhang, J. (2011). Prediction of debris-flow danger area
800 by combining hydrological and inundation simulation methods. *Journal of Mountain*
801 *Science*, 8, 1-9. <https://doi.org/10.1007/s11629-011-2040-8>
- 802 Cui, W. R., Chen, J. G., Chen, X. Q., Tang, J. B., & Jin, K. (2023). Debris flow characteristics
803 of the compound channels with vegetated floodplains. *Science of The Total Environment*,
804 868, 161586. <https://doi.org/10.1016/j.scitotenv.2023.161586>
- 805 [Ding, X. Y., Hu, W. J., Liu, F., & Yang, X. \(2023\). Risk assessment of debris flow disaster in](#)

806 [mountainous area of northern Yunnan province based on FLO-2D under the influence of](#)
807 [extreme rainfall. *Frontiers in Environmental Science*, 11, 1252206.](#)
808 <https://doi.org/10.3389/fenvs.2023.1252206>

809 Eidsvig, U. M. K., Papathoma-Köhle, M., Du, J., Glade, T., & Vangelsten, B. V. (2014).
810 Quantification of model uncertainty in debris flow vulnerability assessment. *Engineering*
811 *Geology*, 181, 15-26. <https://doi.org/10.1016/j.enggeo.2014.08.006>

812 Ettinger, S., Mounaud, L., Magill, C., Yao-Lafourcade, A. F., Thouret, J. C., Manville, V., ... &
813 Llerena, N. M. (2016). Building vulnerability to hydro-geomorphic hazards: Estimating
814 damage probability from qualitative vulnerability assessment using logistic regression.
815 *Journal of Hydrology*, 541, 563-581. <https://doi.org/10.1016/j.jhydrol.2015.04.017>

816 Fuchs, S., Heiss, K., & Hübl, J. J. N. H. (2007). Towards an empirical vulnerability function
817 for use in debris flow risk assessment. *Natural Hazards and Earth System Sciences*, 7(5),
818 495-506. <https://doi.org/10.5194/nhess-7-495-2007>

819 Fuchs, S., Keiler, M., Ortlepp, R., Schinke, R., & Papathoma-Köhle, M. (2019). Recent
820 advances in vulnerability assessment for the built environment exposed to torrential
821 hazards: Challenges and the way forward. *Journal of hydrology*, 575, 587-595.
822 <https://doi.org/10.1016/j.jhydrol.2019.05.067>

823 Gartner, J. E., Cannon, S. H., & Santi, P. M. (2014). Empirical models for predicting volumes
824 of sediment deposited by debris flows and sediment-laden floods in the transverse ranges
825 of southern California. *Engineering Geology*, 176, 45-56.
826 <https://doi.org/10.1016/j.enggeo.2014.04.008>

827 Gorr, A., McGuire, L., & Youberg, A. (2024). Empirical models for postfire debris-flow volume
828 in the southwest United States. *Journal of Geophysical Research: Earth Surface*, 129(11),
829 e2024JF007825. <https://doi.org/10.1029/2024jf007825>

830 Guo, X., Hürlimann, M., Cui, P., Chen, X., & Li, Y. (2024). Monitoring cases of rainfall-induced
831 debris flows in China. *Landslides*, 21(10), 2447-2466. [https://doi.org/10.1007/s10346-](https://doi.org/10.1007/s10346-024-02316-7)
832 [024-02316-7](https://doi.org/10.1007/s10346-024-02316-7)

833 He, K., Hu, X., Wu, Z., Zhong, Y., Zhou, Y., Gong, X., & Luo, G. (2024). Preliminary analysis
834 of the wildfire on March 15, 2024, and the following post-fire debris flows in Yajiang
835 County, Sichuan, China. *Landslides*, 21(12), 3179-3189. [https://doi.org/10.1007/s10346-](https://doi.org/10.1007/s10346-024-02364-z)
836 [024-02364-z](https://doi.org/10.1007/s10346-024-02364-z)

837 Hu, K. H., Cui, P., & Zhang, J. Q. (2012). Characteristics of damage to buildings by debris
838 flows on 7 August 2010 in Zhouqu, Western China. *Natural Hazards and Earth System*
839 *Sciences*, 12(7), 2209-2217. <https://doi.org/10.5194/nhess-12-2209-2012>

840 Jakob, M., Stein, D., & Ulmi, M. (2012). Vulnerability of buildings to debris flow impact.
841 *Natural hazards*, 60, 241-261. <https://doi.org/10.1007/s11069-011-0007-2>

842 Kang, H. S., & Kim, Y. T. (2016). The physical vulnerability of different types of building
843 structure to debris flow events. *Natural Hazards*, 80, 1475-1493.
844 <https://doi.org/10.1007/s11069-015-2032-z>

845 Kean, J. W., Staley, D. M., Lancaster, J. T., Rengers, F. K., Swanson, B. J., Coe, J. A., ... &
846 Lindsay, D. N. (2019). Inundation, flow dynamics, and damage in the 9 January 2018
847 Montecito debris-flow event, California, USA: Opportunities and challenges for post-

848 wildfire risk assessment. *Geosphere*, 15(4), 1140-1163.
849 <https://doi.org/10.1130/ges02048.1>

850 Lee, J. S., Song, C. H., Pradhan, A. M. S., Ha, Y. S., & Kim, Y. T. (2024). Development of
851 structural type-based physical vulnerability curves to debris flow using numerical analysis
852 and regression model. *International Journal of Disaster Risk Reduction*, 106, 104431.
853 <https://doi.org/10.1016/j.ijdr.2024.104431>

854 Luo, H. Y., Zhang, L. M., Zhang, L. L., He, J., & Yin, K. S. (2023). Vulnerability of buildings
855 to landslides: The state of the art and future needs. *Earth-Science Reviews*, 238, 104329.
856 <https://doi.org/10.1016/j.earscirev.2023.104329>

857 Luo, H., Zhang, L., Wang, H., & He, J. (2020). Multi-hazard vulnerability of buildings to debris
858 flows. *Engineering Geology*, 279, 105859. <https://doi.org/10.3389/feart.2022.827438>

859 Marchi L, Arattano M, Deganutti AM (2002) Ten years of debris-flow monitoring in the
860 Moscardo Torrent (Italian Alps). *Geomorphology* 46:1–17. [https://doi.org/10.1016/S0169-
861 555x\(01\)00162-3](https://doi.org/10.1016/S0169-555x(01)00162-3)

862 McGuire, L. A., Ebel, B. A., Rengers, F. K., Vieira, D. C., & Nyman, P. (2024). Fire effects on
863 geomorphic processes. *Nature Reviews Earth & Environment*, 1-18.
864 <https://doi.org/10.1038/s43017-024-00557-7>

865 Navratil, O., Liébault, F., Bellot, H., Travaglini, E., Theule, J., Chambon, G., & Laigle, D.
866 (2013). High-frequency monitoring of debris-flow propagation along the Réal Torrent,
867 Southern French Prealps. *Geomorphology*, 201, 157-171.
868 <https://doi.org/10.1016/j.geomorph.2013.06.017>

- 869 Ouyang, C., Wang, Z., An, H., Liu, X., & Wang, D. (2019). An example of a hazard and risk
870 assessment for debris flows—A case study of Niwan Gully, Wudu, China. *Engineering*
871 *Geology*, 263, 105351. <https://doi.org/10.1016/j.enggeo.2019.105351>
- 872 Ouyang, C., Xiang, W., An, H., Wang, F., Yang, W., & Fan, J. (2023). Mechanistic Analysis and
873 Numerical Simulation of the 2021 Post-Fire Debris Flow in Xiangjiao Catchment, China.
874 *Journal of Geophysical Research: Earth Surface*, 128(1), e2022JF006846.
875 <https://doi.org/10.1029/2022jf006846>
- 876 Papathoma-Köhle, M., Gems, B., Sturm, M., & Fuchs, S. (2017). Matrices, curves and
877 indicators: A review of approaches to assess physical vulnerability to debris flows. *Earth-*
878 *Science Reviews*, 171, 272-288. <https://doi.org/10.1016/j.earscirev.2017.06.007>
- 879 Papathoma-Köhle, M., Schlögl, M., Dosser, L., Roesch, F., Borga, M., Erlicher, M., ... & Fuchs,
880 S. (2022). Physical vulnerability to dynamic flooding: Vulnerability curves and
881 vulnerability indices. *Journal of Hydrology*, 607, 127501.
882 <https://doi.org/10.1016/j.jhydrol.2022.127501>
- 883 Quan Luna, B., Blahut, J., Van Westen, C. J., Sterlacchini, S., Van Asch, T., & Akbas, S. O.
884 (2011). The application of numerical debris flow modelling for the generation of physical
885 vulnerability curves. *Natural hazards and earth system sciences*, 11(7), 2047-2060.
886 <https://doi.org/10.5194/nhess-11-2047-2011>
- 887 Rengers, F. K., McGuire, L. A., Barnhart, K. R., Youberg, A. M., Cadol, D., Gorr, A. N., ... &
888 Kean, J. W. (2023). The influence of large woody debris on post-wildfire debris flow
889 sediment storage. *Natural Hazards and Earth System Sciences*, 23(6), 2075-2088.

890 <https://doi.org/10.5194/nhess-23-2075-2023>

891 Rengers, F. K., McGuire, L. A., Kean, J. W., Staley, D. M., & Hobley, D. E. J. (2016). Model
892 simulations of flood and debris flow timing in steep catchments after wildfire. *Water*
893 *Resources Research*, 52(8), 6041-6061. <https://doi.org/10.1002/2015wr018176>

894 Rickenmann D (1999) Empirical relationships for debris flows. *Nat Hazards* 19:47–77

895 Scheidl, C., & Rickenmann, D. (2010). Empirical prediction of debris-flow mobility and
896 deposition on fans. *Earth Surface Processes and Landforms: The Journal of the British*
897 *Geomorphological Research Group*, 35(2), 157-173. <https://doi.org/10.1002/esp.1897>

898 Si, G. W., Chen, X. Q., Chen, J. G., Zhao, W. Y., Li, S., & Li, X. N. (2022). Failure criteria of
899 unreinforced masonry walls of rural buildings under the impact of flash floods in
900 mountainous regions. *Journal of Mountain Science*, 19(12), 3388-3406.
901 <https://doi.org/10.1007/s11629-022-7491-6>

902 Sichuan Hydrological Manual (1984) Rainstorm-runoff calculation method in small watershed,
903 1984, Sichuan Water Conservancy and Power Department. Electronic publishing.

904 Thomas, M. A., Kean, J. W., McCoy, S. W., Lindsay, D. N., Kostelnik, J., Cavagnaro, D. B., ...
905 & Collins, B. D. (2023). Postfire hydrologic response along the Central California (USA)
906 coast: insights for the emergency assessment of postfire debris-flow hazards. *Landslides*,
907 20(11), 2421-2436. <https://doi.org/10.1007/s10346-023-02106-7>

908 Totschnig, R., Sedlacek, W., & Fuchs, S. (2011). A quantitative vulnerability function for fluvial
909 sediment transport. *Natural Hazards*, 58, 681-703.

910 Vahedifard, F., Abdollahi, M., Leshchinsky, B. A., Stark, T. D., Sadegh, M., & AghaKouchak,

- 911 A. (2024). Interdependencies between wildfire-induced alterations in soil properties, near-
912 surface processes, and geohazards. *Earth and Space Science*, 11(2), e2023EA003498.
913 <https://doi.org/10.1029/2023ea003498>
- 914 Wang, T., Chen, J., Chen, X., You, Y., & Cheng, N. (2018). Application of incomplete similarity
915 theory to the estimation of the mean velocity of debris flows. *Landslides*, 15, 2083-2091.
916 <https://doi.org/10.1007/s10346-018-1045-6>
- 917 Wang, T., Yin, K., Li, Y., Chen, L., Xiao, C., Zhu, H., & van Westen, C. (2024). Physical
918 vulnerability curve construction and quantitative risk assessment of a typhoon-triggered
919 debris flow via numerical simulation: A case study of Zhejiang Province, SE China.
920 *Landslides*, 21(6), 1333-1352. <https://doi.org/10.1007/s10346-024-02218-8>
- 921 Yang, Y., Hu, X., Han, M., He, K., Liu, B., Jin, T., ... & Huang, J. (2022). Post-fire temporal
922 trends in soil properties and revegetation: Insights from different wildfire severities in the
923 Hengduan Mountains, Southwestern China. *Catena*, 213, 106160.
924 <https://doi.org/10.1016/j.catena.2022.106160>
- 925 Yang, H., Liu, J., Sun, H., You, Y., Zhao, W., & Yang, D. (2024). Evolution characteristics of
926 post-fire debris flow in Xiangjiao gully, Muli County. *Catena*, 246, 108353.
927 <https://doi.org/10.1016/j.catena.2024.108353>
- 928 Zhang, B., Zhang, G., Fang, H., Wu, S., & Li, C. (2024). Risk assessment of flash flood under
929 climate and land use and land cover change in Tianshan Mountains, China. *International
930 Journal of Disaster Risk Reduction*, 115, 105019.
931 <https://doi.org/10.1016/j.ijdrr.2024.105019>

- 932 Zhang, S., Zhang, L., Li, X., & Xu, Q. (2018). Physical vulnerability models for assessing
933 building damage by debris flows. *Engineering Geology*, 247, 145-158.
934 <https://doi.org/10.1016/j.enggeo.2018.10.017>
- 935 Zhou, B.F., Li, D.J., Luo, D.F., Lv, R.R., Yang, Q.X., 1991. Guide to Prevention of Debris Flow.
936 Beijing, China.
- 937 [Zhang, W., Chen, J., Ma, J., Cao, C., Yin, H., Wang, J., & Han, B. \(2023\). Evolution of sediment
938 after a decade of the Wenchuan earthquake: a case study in a protected debris flow
939 catchment in Wenchuan County, China. *Acta Geotechnica*, 18\(7\), 3905-3926.
940 <https://doi.org/10.1007/s11440-022-01789-x>](#)